Bioorganic Chemistry 169 (2026) 109393

Contents lists available at ScienceDirect

Bioorganic Chemistry

journal homepage: www.elsevier.com/locate/bioorg

Cytotoxicity, apoptosis, molecular docking, and molecular dynamics study of novel compounds of Sulfamide derivatives coupled with DHP scaffolds as potent inhibitors of the MCF-7, A549, SKOV-3, and EA. yh926 carcinoma cells

Amjed Abdulrasool [a], Aymen G. Faisel [b], Ruaa Q. Ibrahim [c], Tahseen A. Alsalim [c], Dunya AL-Duhaidahawi [d], Ahmed A. Majed [c,**], Nehad H. Gad [e], Mohammad Y. Alfaifih [f,g,h], Ali A. Shatii [f,g,h], Serag Eldin I. Elbehairii [f,g,h], Ahmed M. Hussein [i], Fatih Alioglu [i], Mohammed Aufy [i,j,*]

[a] Department of Surgery, Kolding hospital, Sygehusvej 24, 6000, Kolding, Denmark
[b] Department of Applied Marine Sciences, College of Marine Sciences, University of Basrah, Basrah 61001, Iraq
[c] Department of Chemistry, College of Education for Pure Sciences, University of Basrah, Basrah 61001, Iraq
[d] College of Pharmacy, University of Kufa, AL-Najaf, Iraq
[e] Forensic Medicine and Clinical Toxicology Department, Faculty of Medicine Alexandria University, Egypt
[f] Central Labs, King Khalid University, Alqura'a, Abha, Saudi Arabia
[g] Biology Department, Faculty of Science, King Khalid University, Abha, Saudi Arabia
[h] Tissue Culture and Cancer Biology Research Laboratory, King Khalid University, Abha, Saudi Arabia
[i] Department of Pharmaceutical Sciences, Division of Pharmacology and Toxicology, University of Vienna, Vienna, Austria
[j] Department of Pharmaceutical Sciences, Division of Pharmaceutical Chemistry, University of Vienna, Vienna, Austria

ARTICLE INFO

Keywords:
DHP
Sulphamide drug
Anticancer
Apoptosis
Cell cycle
MCF-7
A549
SKOV-3

ABSTRACT

A novel series of dihydropyridine-sulfonyl derivatives (AG-CHO and analogues A1–A7) were synthesized and structurally characterized. Molecular docking demonstrated favorable binding of these compounds to autophagy-associated and cancer-related targets, while molecular dynamics simulations confirmed A5 as the most stable ligand protein interactions. Functional assays in SKOV-3, MCF-7, A549, and EA.hy.926 cells using acridine orange staining and flow cytometry revealed significant autophagy induction. Among all tested compounds AG-CHO emerged as the most potent inducer of autophagy. Notably, derivatives such as A6 and A7 showed selective potency in endothelial cells, whereas A1, A5, and A7 were effective in A549 cells, indicating cell-specific activity. Collectively, this integrated computational and experimental study identifies A5 as the lead compound and highlights dihydropyridine-sulfonyl scaffolds as promising autophagy modulators and potential anticancer candidates for further preclinical development.

1. Introduction

Cancer is a complex and deadly disease that impacts many people in the world. When any organ of the body develops cancer, there are several possible causes such as genetics, environmental factors, and lifestyle habits [1–3]. Cancer is among the most significant modern health issues, as it can affect human health on a global scale. According to The World Health Organization (2023), cancer kills nearly 10 million individuals per year the second most common cause of death. [4]. In addition to the physical symptoms of cancer, it is also associated with a substantial psychosocial and economic burden. The disease is characterized by unregulated cell growth that interferes with the normal functioning of organs and can spread to other sites [5,6]. Mortality rates also differ among cancer types, with lung, colorectal, liver, and breast cancer being responsible for the most deaths [7]. The types of treatments for cancer that are offered have changed significantly over the past few

* Corresponding author at: Department of Pharmaceutical Sciences, Division of Pharmacology andToxicology, University of Vienna, Vienna, Austria
** Corresponding author.
E-mail addresses: eduppg.ahmed.majed@uobasrah.edu.iq (A.A. Majed), mohammed.aufy@univie.ac.at (M. Aufy).

https://doi.org/10.1016/j.bioorg.2025.109393
Received 9 October 2025; Received in revised form 29 November 2025; Accepted 14 December 2025
Available online 16 December 2025

decades, as advances in precision medicine have transformed how many patients are managed. Targeted agents directed at specific molecular abnormalities have improved survival and may decrease systemic toxicity compared to traditional cytotoxic chemotherapy [8–10]. Dihydropyridines, a large class of heterocyclic compounds central to many bioactive natural and synthetic compounds, have attracted considerable attention over the last years [11]. Many of them, such as Amlodipine, Barnidipine, Lacidipine, and Manidipine, are approved drugs [12–15]. There are many synthetic routes to dihydropyridines. The classical Hantzsch synthesis remains the most common method, even though it was discovered at the end of the 19th century [16,17]. It is a multicomponent reaction which condenses an aldehyde with two equivalents of a β-keto ester in the presence of ammonia or a source of amine. A new procedure for the synthesis of dihydropyridines has been developed that can complete reactions in a fraction of the time and with higher yields by using a catalyst. Microwave irradiation and by sonication [18–20]. 1,4-DHP compounds were synthesized by using β-keto ester compounds and their derivatives. A series of symmetrical 1,4-dihydropyrimidine derivatives has been developed using a four component reaction involving the in situ generation of β-ketoesters via trans esterification, followed by the one-pot Hantzsch reaction with aryl aldehyde and ammonium acetate [21–24]. A significant class of synthetic antimicrobial medications, sulfonamides or sulfanilamides are employed pharmacologically as broad spectrum treatments [25]. Sulfonamide derivatives are among the first synthetic antibacterial agents, and the first sulfa drug was discovered by Gerhard Domagk in the 1930s [26,27]. In recent years, sulfa derivatives were found to have anticancer [28,29], antiviral [30], and anti-inflammatory properties. Sulfa-based agents have different modes of action which include dihydropteroate synthase inhibition [31], carbonic anhydrase inhibition [32], and cyclooxygenase modulation. Structure-activity relationship studies resulted in sulfa drug derivatives with different potencies and reduced toxicity for different applications [33]. In this study, we employed a scaffold-hybridization strategy to design novel sulfamide-dihydropyridine (DHP) derivatives as potential multitarget anticancer agents. The DHP core, a π-rich bioactive scaffold, was selected for its capacity to engage in hydrophobic and π-π interactions, while the sulfamide moiety a sulfonamide bio-isostere was incorporated to enhance hydrogen-bonding potential, polarity, and solubility. Combining these two pharmacophores was intended to improve target binding affinity and promote apoptosis induction. Electronic and steric modifications at DHP C3/C5 and aryl positions were designed to fine-tuned molecular interactions, while computational studies, including molecular docking and dynamics simulations, were employed to evaluate predicted binding stability prior to synthesis. This hybridization was complemented by previous works of bioactive sulfonamide-DHP analogues characterization [34–41], and this has reinforced the chemical feasibility of such molecular design. Subsequently, synthesized sulfamide-DHP derivatives were characterized by spectroscopic methods as well as their cytotoxicity, apoptotic induction, molecular docking behavior and molecular dynamics with respect to MCF-7 (breast), A549 (lung), SKOV-3 (ovarian) and EA.hy926 (endothelial) carcinoma cell lines. The present work is focused on analysing the structure–activity relationships of these hybrid molecules and their potential use as leading anticancer drug candidates. The next figure shows the chemical structures of the sulfamide-dihydropyridine (DHP) derivatives that were synthesized by scaffold-hybridization and identifies the crucial stages of synthesis.

2. Material and methods

2.1. Instrumentation and spectral measurements

Chemical reagents and solvents were purchased from Fischer, Sigma, and Merck. DMSO-d_6 was used as the solvent and Si $(CH_3)_4$ (TMS) was used as internal standard. The Shimadzu FTIR (affinity-1) was used to record the infrared spectra in the range of 4000–400 cm^{-1}. The EI mass spectra were measured using Agilent 7945 mass spectrometer. The ^1H and ^{13}C NMR spectra were measured using Brucker 400 spectrometer. The chemical shift (δ) and coupling constants were measured in parts per million (ppm). Elemental analysis (CHNS) was measured by using elementary *Vario* MICRO.

2.2. Chemistry section

2.2.1. Synthesis procedure of ethyl 2-methyl-4-(3-nitrophenyl)-6-oxo-1,4,5,6-tetrahydro pyridine-3-carboxylate (AG) [34]

A mixture of ethyl acetoacetate (1.30 g, 10 mmol), 3-nitrobenzaldehyde (1.51 g, 10 mmol), Meldrum's acid (1.44 g, 10 mmol), and ammonium acetate NH4OAc (0.809 g, 10.5 mmol) in glacial acetic acid (10 mL) was heated under reflux for 12 h and monitored by TLC, benzene: methanol (2:8 *v*/v). After the mixture cooled, the solid product was collected by filtration and recrystallized from methanol.

White powder, recrystallized from Methanol, yield 64 %, m.p. 204-205 °C, $R_f = 0.81$. IR (KBr, υ, cm^{-1}): 3234 (NH str.), 3132 (CH-Ar.), 2918 (CH-aliphatic), 1697, 1631 (C═O), 1597 (C═C) and 1350, 1550 (NO_2). ^1H NMR (400 MHz, δ; ppm); 10.07(1H, s,NH),8.09–7.63 (4H,Ar-H), 4.30 (H, d, $J = 8$, CH-DHP), 4.01 (2H, q, $J = 8$,OCH_2), 3.02, 2.47(2H, CH_2, d, $J = 8$,H13,14 DHP), 2.35(3H,s,CH_3-DHP), 1.09(3H, t, $J = 8$, CH_2-$\underline{CH_3}$). ^{13}C NMR (100 MHz, DMSO-d_6, δ, ppm) 18.72(CH_3, C17),14.5(CH_3-C21),38.17, 37.62(C11,12), 60(CH_2, C20),121–148.5 (Ar—C), 149.49 (C8), 104.54(C7), 169.8(C═O amide), 166.68(C═O ester). MS: EI (70 eV, *m/z*): $M^+ = 304$(25.4 %) and 306(M^++2), the base peak =287(100 %), and the fragments: 259, 231, 185, 115 and 76. Anal. calc. For $C_{15}H_{16}N_2O_5$: C, 59.205, H, 5.300, N, 9.206. found: C, 58.925, H, 5.193, N, 9.107.

2.2.2. Synthesis of ethyl 6-chloro-5-formyl-2-methyl-4-(3-nitrophenyl)-1,4-dihydropyridine-3-carboxylate. (AG-CHO)

The mixture of anhydrous DMF (1.24 mL, 16 mmol) and dry DCM (4 mL) was added dropwise to phosphorus oxychloride ($POCl_3$) (1.5 mL, 16 mmol) with stirring in the reaction vessel at room temperature for 30 min. Then the solution of 6-oxo-1,4,5,6-tetrahydropyridine-3-carboxylate (AG) (1.216 g, 4 mmol) in 16 mL of dry DCM was added. After 24 h stirring at room temperature, a solution of (16 g of sodium acetate (NaOAc) in 24 mL of water was added slowly with continued stirring for 1 h. The reaction monitored by TLC, benzene: methanol (2:8 *v*/v). The product was extracted by DMC three times, and then dried with sodium sulfate, and the solvent was removed under reduced pressure.

Light yellow precipitate, recrystallized from Methanol, yield 68 %, m.p., 213-214 °C, $R_f = 0.85$. IR (KBr, υ, cm^{-1}): 3323 (NH str.), 3078 (CH-Ar.), 2928 (CH-aliphatic), 2854, 2762 (CH-Aldehyde), 1701, 1649 (C═O), 1601 (C═C) and 1348, 1527 (NO_2). ^1H NMR (400 MHz, δ; ppm); 10.52(1H, s, NH), 9.68 (H, s, CHO), 8.04–7.57(4H, Ar—H), 5.04 (H, s, CH-DHP), 4.01(2H, q, $J = 8$, OCH_2), 2.36(3H, s, CH_3-DHP), 1.11 (3H, t, $J = 8$, CH_2-$\underline{CH_3}$). ^{13}C NMR (100 MHz, DMSO-d_6, δ, ppm, *J;* Hz) δ-14.8 (CH_3),18.3 ($\underline{CH_3}$-DHP), 38.4 (C6-DHP), 60.2 (OCH_2), 110–148.5 (Ar—C),146, 143(C2, C4-DHP), 187(C═O Aldehyde),166.6 (C═O ester). MS: EI (70 eV, *m/z*), $M^+ = 350$(12.75 %) and 352(M^++2), the base peak =228(100 %), and the fragments: 333, 277, 200, 131 and 76. Anal. calc. For $C_{16}H_{15}ClN_2O_5$: C, 54.788, H, 4.310, N, 7.987. found: C, 54.503, H, 4.207, N, 7.625.

2.2.3. General procedure of the synthesis of sulfa drug-bearing DHP derivatives (A1-A7) [35]

A mixture of 1,4-dihydropyridine (AG-CHO) (0.70 g, 2 mmol) and sulfa drug derivatives (2 mmol) was dissolved in ethanol (10 mL); 1 mL glacial acetic acid as a catalyst was added. The mixture was heated under reflux for 12 h and monitored by TLC hexane: ethyl acetate (5:5 *v*/v). A colored solid product was separated by cooling, and the product was filtered and recrystallized from the appropriate solvent.

*2.2.3.1. Ethyl(E)-6-chloro-2-methyl-5-(((4-(N-(5-methylisoxazole-3-yl) sulfamoyl) phenyl) imino) methyl)-4-(3-nitro phenyl)-1,4-dihydropyridine-3-carboxylate **(A1)***. Yellow powder, recrystallized from methanol, yield 73 %, m.p.189-191 °C, R_f = 0.68. IR (KBr, υ, cm^{-1}): 3392 s (NH str.), 3080 (CH-Ar.), 2981 (CH-aliphatic), 1668 (C═O),1631 (HC═N), 1597 (C═C) and 1360, 1165 (SO_2). ^{1}H NMR (400 MHz, *δ;* ppm, *J*; Hz); 11.26 (s, 1H, NH sulfa),10.60(s, 1H, NH DHP),8.88(s, 1H, —CH═N),8.02–7.39 (m, 8H, Ar—H),6.13(s, 1H, H—C═N isoxazole),4.95(s, 1H, C4-DHP),4.01(q, 2H, *J* = 8, OC$\underline{H}_2$CH$_3$),2.29(s, 3H, C$\underline{H}_3$-DHP),2.11(s, 3H, C$\underline{H}_3$-methoxazole),1.11(t, 3H, *J* = 8 Hz, OCH$_2$C$\underline{H}_3$). ^{13}C NMR (100 MHz, DMSO-d_6, *δ,* ppm) *δ*- 12.4 (CH_3-Oxazole),14.5 (CH_3),18.6 (CH_3-DHP),42.4, (C6-DHP), 59.9 (OCH_2),95–153.5(Ar—C),101, 103.9 (C1, C5),133(C4), 140.3 (C2),161 (C═N), 161(C═N Oxazole),166.6 (C═O ester). MS: EI (70 eV, *m/z*): M^+; $[C_{26}H_{24}ClN_5O_7S]^+$; 585(7.5 %) and 587 ($M^+$+2), the base peak$[C_5H_5]^+$ = 65(100 %), and the fragments: 452, 237, 191, 92 and 76. Anal. calc. For $C_{26}H_{24}ClN_5O_7S$: C, 53.288, H, 4.128, N, 11.954. S, 5.471.found: C, 52.914, H, 4.002, N, 11.761. S, 5.297.

*2.2.3.2. Ethyl(E)-6-chloro-2-methyl-5-(((4-(N-(−thiazol-2-yl) sulfamoyl) phenyl) imino) methyl)-4-(3-nitrophenyl)- 1,4-dihydropyridine-3-carboxylate **(A2)***. Orange crystals, recrystallized from Methanol, yield 66 %, m.p. 213-215 °C, Rf = 0.65. IR (KBr, υ, cm^{-1}): 3406 (NH str.), 3049 (CH-Ar.), 2953 (CH-aliphatic), 1672 (C═O),1631 (HC═N), 1595 (C═C) and 1350, 1141 (SO_2). ^{1}H NMR (400 MHz, *δ*; ppm, *J*; Hz); 12.63(s, 1H, NH sulfa),10.56(s, 1H, NH DHP),8.79(s, 1H, -CH═N),8.27–7.24(m, 8H, Ar—H),6.81(d, 2H, thiazole ring),4.95(s, 1H, C4-DHP),4.01(s, 2H, OC$\underline{H}_2$CH$_3$),2.35(s, 3H, C$\underline{H}_3$-DHP), 1.12(s, 3H, OCH$_2$C$\underline{H}_3$). ^{13}C NMR (100 MHz, DMSO-d_6, *δ*, ppm) -14.5 (CH_3), 18.6 (CH_3-DHP), 42.9 (C6-DHP), 59.9 (OCH_2), 149.8–108.5 (Ar—C), 100.8, 108.5 (C1, C5), 130.7 (C4), 142.19 (C2), 160.8(C═N), 169.0 (C═N Thiazole), 166.4 (C═O ester). MS: EI (70 eV, *m/z*): M^+-$[C_{25}H_{22}ClN_5O_6S_2]^+$ = 587(9.5 %) and 589(M^++2), the base peak$[C_6H_5N]^+$ = 92(100 %), and the fragments: 523, 413,209, 191, 149, 108 and 69. Anal. calc. For $C_{25}H_{22}ClN_5O_6S_2$: C, 51.061, H, 3.771, N, 11.910. S, 10.904. Found: C, 50.817, H, 3.582, N, 11.659. S, 10.841.

*2.2.3.3. Ethyl(E)-6-chloro-2-methyl-5-(((4-(N-(pyrimidine-2-yl) sulfamoyl) phenyl) imino) methyl)-4-(3-nitro phenyl)-1,4-dihydropyridine-3-carboxylate **(A3)***. Orange powder, recrystallized from Methanol, yield 58 %, m.p. 223-226 °C, R_f = 0.6. IR (KBr, υ, cm^{-1}): 3390 s (NH str.), 3043 (CH-Ar.), 2937 (CH-aliphatic), 1666 (C═O),1631 (HC═N), 1593 (C═C),1340, 1141 (SO_2) and 939 (S—N). ^{1}H NMR (400 MHz, *δ*; ppm., *J*; Hz); 11.48(s, 1H, NH sulfa),10.56(s, 1H, NH of DHP),8.48(s, 1H, -CH═N),8.11–7.02(m, 11H, Ar—H),4.95(s, 1H, C4-DHP),4.01(s, 2H, OC$\underline{H}_2$CH$_3$),2.35(s, 3H, C$\underline{H}_3$-DHP),1.12(s, 3H, OCH$_2$C$\underline{H}_3$). ^{13}C NMR (100 MHz, DMSO-d_6, *δ*, ppm) - 14.5 (CH_3), 18.6 (CH_3-DHP), 42.9 (C6-DHP), 59.9 (OCH_2), 150.6–112.5 (Ar—C), 101.3, 103.9 (C1, C5), 129.9 (C4), 135.5 (C2), 158.8 (C═N), 170.09 (C═N pyrimidine), 166.40 (C═O ester). MS: EI (70 eV, *m/z*): M^+-$[C_{26}H_{23}ClN_6O_6S]^{+\cdot}$ =582(7.15 %) and 584(M^++2), the base peak$[C_5H_5]^+$ = 65(100 %), and the fragments: 477, 413,276, 191, 92,76 and 45. Anal. calc. For $C_{26}H_{23}ClN_6O_6S$: C, 53.562, H, 3.976, N, 14.416. S, 5.499. Found: C, 53.317, H, 3.791, N, 14.208. S, 5.273.

*2.2.3.4. Ethyl(E)-6-chloro-2-methyl-5-(((4-(N-(pyridine-2-yl) sulfamoyl) phenyl) imino) methyl)-4-(3-nitrophenyl) -1,4-dihydropyridine-3-carboxylate **(A4)***. Orange crystal, recrystallized from ethanol, yield 62 %, m.p. 218-220 °C, R_f = 0.62. IR (KBr, υ, cm^{-1}): 3244 s (NH str.), 3074 (CH-Ar.), 2980 (CH-aliphatic), 1666 (C═O),1631 (HC═N), 1590–1575 (C═C),1350, 1149 (SO_2) and 1350,1527 (NO_2). ^{1}H NMR (400 MHz, *δ*; ppm, *J*; Hz); 11.66(s, 1H, NH sulfa),10.57(s, 1H, NH DHP), 8.85(s, 1H, -CH═N),8.11–6.87(m, 12H, Ar—H),4.94(s, 1H, DHP), 4.02(s, 2H, OC$\underline{H}_2$CH$_3$) 2.35(s, 3H, C$\underline{H}_3$-DHP),1.10(s, 3H, OCH$_2$C$\underline{H}_3$). ^{13}C NMR (100 MHz, DMSO-d_6, *δ*, ppm) – 14.5 (CH_3), 18.6(CH_3-DHP), 42.9(C6-DHP), 59.9 (OCH_2), 153.2–108.9(Ar—C), 101.1, 103.9(C1, C5), 135.1 (C4), 142.0(C2), 161.1 (C═N), 170.0 (C═N pyrimidine), 166.6 (C═O ester). MS: EI (70 eV, *m/z*): M^+-$[C_{27}H_{24}ClN_5O_6S]^+$ = 581(5.8 %) and 583 (M^++2), the base peak$[C_7H_7SO_2N_2]^+$ = 184(100 %), and the fragments: 504, 321,276, 92,76 and 65. Anal. calc. For $C_{27}H_{24}ClN_5O_6S$: C, 55.717, H, 4.156, N, 12.033. S, 5.509.found: C, 55.471, H, 3.985, N, 11.912. S, 5.309.

*2.2.3.5. Ethyl(E)-6-chloro-2-methyl-5-(((4-(N-(4-methylpyrimidine-2-yl) sulfamoyl) phenyl) imino) methyl)-4-(3- nitrophenyl) -1,4-dihydropyridine-3-carboxylate **(A5)***. Orange powder, recrystallized from methanol, yield 76 %, m.p. 247-249 °C, R_f = 0.65. IR (KBr, υ, cm^{-1}): 3209(NH str.), 3080 (CH-Ar.), 2935(CH-aliphatic), 1672(C═O),1631 (HC═N), 1593 (C═C),1348, 1154 (SO_2) and, 1350,1527 (NO_2). ^{1}H NMR (400 MHz, *δ*; ppm, *J*; Hz); 11.54(s, 1H, NH sulfa),10.56(s, 1H, NH DHP),8.89(s, 1H, -CH═N),8.31–7.34(m, 10H, Ar—H),4.95(s, 1H, C4-DHP),4.01(q, 2H, *J* = 8 Hz, OC$\underline{H}_2$CH$_3$),2.35(s, 3H, C$\underline{H}_3$-DHP),2.31(s, 3H, C$\underline{H}_3$-pyrimidine ring),1.11(t, 3H, *J* = 8 Hz, OCH$_2$C$\underline{H}_3$). ^{13}C NMR (100 MHz, DMSO-d_6, *δ*, ppm) - 14.5 (CH_3),18.6(CH_3-DHP),23.7 (CH_3-Pyridine- C40), 42.9 (C6-DHP), 59.9(OCH_2), 153.5–112.4(Ar—C), 101.34, 103.97(C1, C5), 130.73(C4), 141.95(C2), 157.07 (C═N), 169.95(C═N pyridine), 166.67 (C═O ester). MS: EI (70 eV, *m/z*): M^+-$[C_{27}H_{26}ClN_6O_6S]^+$ = 596 (3.8 %) and 598(M^++2), the base peak$[C_{11}H_7N_4]^+$ = 199(100 %), and the fragments: 504, 276, 171,92,76 and 65. Anal. calc. For $C_{27}H_{25}ClN_6O_6S$: C, 54.315, H, 4.220, N, 14.077. S, 5.370.found: C, 53.977, H, 4.047, N, 13.903. S, 5.184.

*2.2.3.6. Ethyl(E)-5-(((4-(N-acetyl sulfamoyl) phenyl) imino) methyl)-6-chloro-2-methyl-4-(3-nitrophenyl)-1,4-dihydropyridine −3-carboxylate **(A6)***. Orange crystal, recrystallized from ethyl acetate, yield 71 %, m.p. 192-194 °C, Rf = 0.7. IR (KBr, υ, cm^{-1}): 3209 s (NH str.), 3080 (CH-Ar.), 2980 (CH-aliphatic), 1707 (C═O),1655(C═O amide),1631 (HC═N), 1595 (C═C),1348, 1159 (SO_2). ^{1}H NMR (400 MHz, *δ*; ppm, *J*; Hz); 12.53 (s, 1H, NH sulfa),10.57(s, 1H, NH DHP),8.91(s, 1H, -CH═N),8.11–7.37 (m, 8H, Ar—H), 4.95(s, 1H, C4-DHP),4.01(q, 2H, *J* = 8, OC$\underline{H}_2$CH$_3$), 2.35 (s, 3H, C$\underline{H}_3$-DHP), 1.90(s, 3H, C$\underline{H}_3$-C═O), 1.12(t, 3H, *J* = 8, OCH$_2$C$\underline{H}_3$). ^{13}C NMR (100 MHz, DMSO-d_6, *δ*, ppm) - 14.5(CH_3), 18.67 (CH_3-DHP), 21.9 (CH_3CO), 42.9 (C6-DHP), 60.0(OCH_2), 149.8–115.5(Ar—C), 101.34, 103.9 (C1, C5), 137.5 (C4), 142.2(C2), 160.4(C═N), 176.7 (C═O amide of sulfa.), 166.5 (C═O ester). MS: EI (70 eV, *m/z*):M^+-$[C_{24}H_{23}ClN_4O_7S]^{+\cdot}$ =581(4 %) and 583(M^++2), the base peak$[C_5H_5]^+$ = 65(100 %), and the fragments: 519, 474,321, 154,76 and 50. Anal. calc. For $C_{24}H_{23}ClN_4O_7S$: C, 52.699, H, 4.238, N, 10.244. S, 5.862. Found: C, 52.527, H, 4.062, N, 9.909. S, 5.770.

*2.2.3.7. Ethyl(E)-6-chloro-2-methyl-4-(3-nitrophenyl)-5-(((4-sulfamoyl phenyl) imino) methyl)-1,4-dihydropyridine-3-carboxylate **(A7)***. Yellow crystal, recrystallized from Ethanol, yield 79 %, m.p. 195-196 °C, Rf = 0.72. IR (KBr, υ, cm^{-1}): 3376, 3215 (NH_2), 3215 (NH str.), 3080 (CH-Ar.), 2978 (CH-aliphatic), 1707 (C═O),1655(C═O amide),1627 (HC═N), 1596 (C═C),1344, 1150 (SO_2). ^{1}H NMR (400 MHz, *δ*; ppm, *J*; Hz); 12.55(s, 2H, NH sulfa),10.57(s, 1H, NH DHP), 8.88(s, 1H, -CH═N),8.14–7.23(m, 8H, Ar—H), 4.97(s, 1H, C4-DHP), 4.01(q, 2H, *J* = 8, OC$\underline{H}_2$CH$_3$), 2.36(s, 3H, C$\underline{H}_3$-DHP),1.13(t, 3H, *J* = 8, OCH$_2$C$\underline{H}_3$). ^{13}C NMR (100 MHz, DMSO-d_6, *δ*, ppm) - 14.5 (CH_3), 18.6 (CH_3-DHP), 42.9 (C6-DHP), 60.0 (OCH_2), 149.8–115.5 (Ar—C), 100.8, 103.9 (C1, C5), 137.5 (C4), 142.2 (C2), 163.2 (C═N), 166.7 (C═O ester). MS: EI (70 eV, *m/z*): M^+-$[C_{22}H_{21}ClN_4O_6S]^{+\cdot}$ =504(5 %) and 506(M^++2), the base peak $[C_5H_5]^+$ = 65(100 %), and the fragments: 424, 287,156, 104,92,80 and 50. Anal. calc. For $C_{22}H_{21}ClN_4O_6S$: C, 52.329, H, 4.192, N, 11.096. S, 6.350.found: C, 52.117, H, 4.054, N, 10.938. S, 6.179.

2.3. Pharmacology network

We built a bipartite network to map and study links between chemical compounds and their predicted protein targets. In this design: Nodes stood for either a compound or a target protein while edges represented predicted interactions between a compound and a protein target. The team created the network with Network X in Python and then loaded it into Cytoscape to inspect the overall shape of the landscape. Clusters of closely linked proteins and prominent hub nodes were spotted both by eye and through automated analysis. To find the proteins that truly drive the network, we ran a set of standard graph tests, focusing on three main pieces: Degree centrality-how many immediate partners each protein has – Betweenness centrality-how often a protein acts as a bridge between clusters - Closeness centrality-how quickly one protein can reach all the others in the graph Although we looked at all three, we ranked the proteins mainly by degree centrality because a high count of direct links signals broad interaction with many compounds and marks a protein as a likely drug-discovery target. After running the centrality scan, we pulled out and graphed the highest-ranking targets, then visualisation and interpretation of the compounds-target interaction network as a force -directed graph to highlight key clusters interaction hubs. Nodes representing high-degree proteins were visibly larger and more central, consistent with their computed scores. In parallel, a bar graph was generated to illustrate the relative importance of the top 10 proteins.

2.4. Insilico pharmacokinetic studies

2.4.1. ADMET study

The ADMET profiling of compounds (A1–A7) was carried out with the Swiss ADME web platform, which integrates several computational methods to estimate various pharmacokinetic and medicinal chemistry properties. Compound structures were input as SMILES strings, and the tool provided information on physicochemical properties, solubility, permeability, cytochrome P450 inhibition and drug-likeness according to scientific rules including Lipinski's, Ghose's and Veber's rules. ESOL, Ali and SILICOS-IT models were employed to predict the aqueous solubility, and GI absorption, BBB permeation and cytochrome enzyme inhibition profiles.

2.5. Molecular docking studies

Molecular docking studies were performed using Auto Dock 4.2 to predict the binding interactions between the target protein AKT1 and the selected ligands. The protein structure (PDB ID: AKT1) was obtained from Protein Data Bank, and all water molecules, heteroatoms, and co-crystalized were removed using Auto Dock tools (ADT). Polar hydrogen atoms were added, and Kollman charges were assigned to prepare the protein for docking. For ligand preparation, 2D structures were drawn in ChemDraw2020 and converted into 3D format using Open Babel [34,35]. The ligands were energy-minimized using the MMFF94 force field to obtain stable conformations. Gasteiger charges were introduced, and rotatable bonds formulated in ADT. A grid box was positioned to cover the active site of AKT1, defining the region where docking would take place. Docking simulations were done using Lamarckian Genetic Algorithm (LGA). For each ligand, a spectrum of up to eight conformations were generated, thus ensuring a robust exploration of the binding space. The ligands were re-docked to confirm, and their outcomes cross-verified. Docked complexes obtained were ranked according to binding energy (ΔG), where the best pose for each ligand had the lowest binding energy and most favorable interactions and was selected for further analysis. Discovery studio Visualizer was used to analyze and visualize hydrogen bonds, hydrophobic interactions and π-π stacking interactions between the ligands and AKT1.

2.6. Molecular dynamics (MD)

Molecular dynamics simulations were performed using the Desmond module in the Schrodinger suite (2023) to assess the stability and dynamic behavior of the protein-ligand complex under physiological conditions (310 k, 1 atm). The protein ligand complex obtained from molecular docking was prepared using the protein preparation wizard in Schrodinger Maestro interface. Missing hydrogen atoms were added, bond orders were assigned, and the protonation states of residues were adjusted to PH 7.0 using Epik. The complex was energy-minimized using OPLS4 force field. The prepared complex was placed in an orthorhombic simulation box with a 10 Å buffer distance in all directions. The system was solvated using the TIP3P water model and counterions (Na^+ or Cl^-) were added to neutralize the system. A salt solution (0.15 M NaCl) was incorporated here to mimic physiological ionic strength. The system first underwent energy minimization within about 30 min to remove bad contacts. Following this, there was a multi-stage equilibration protocol from the Desmond package consisting of restrained NVT and NPT ensembles that gradually relaxed the system to the simulation conditions of 300 K and 1 atm. For the production run, a 100 ns MD baseline simulation was performed in NPT ensemble under constant temperature and pressure regulated by Nosé–Hoover and Martyna–Tobias–Klein barostats. A time step of 2 fs was used with coordinates stored every 100 ps. The trajectories were processed and analyzed using SID and Maestro tools for biochemical trajectories. The Evaluation of the complex stability and its binding behavior with time, key parameters such as root mean square deviation (RMSD), root mean square fluctuation (RMSF), radius of gyration (Rg), hydrogen bond occupancy, and timelines of ligand-protein interactions were calculated.

2.7. MTT cell viability assay

The cytotoxic effect of the compounds (A1–7) was evaluated using MTT assay where cells seeded in 96-well plates at a density of 5×10^3 cells/well and allowed to adhere overnight under standard culture conditions (37 °C, 5 % CO2). The following day, cells were treated with different concentrations of the test compounds for 24–48 h. After incubation, 20 μL of MTT solution (5 mg/mL in PBS) was added to each well and plates were incubated for 4 h at 37 °C to allow mitochondrial dehydrogenases to convert MTT into soluble purple formazan crystals. The medium was carefully aspirated, and the formazan was dissolved in 150 μL of DMSO. Absorbance was measured at 570 nm using a microplate reader, with a reference wavelength of 630 nm. Cell viability was expressed as percentage relative to untreated control cells, and IC50 values were calculated using nonlinear regression analysis.

2.8. Cell cycle analysis

Human cancer cells (A549, MCF-7, SKOV-3, and Ea-yh926) were inoculated in a 6-well plate and allowed to adhere for 24 h. The cells were then exposed to IC50 doses of previously determined manufactured DHP sulfamide compounds (AG-CHO, A1, A2, A3, A5, A6, and A7), followed by 48 h of incubation. Subsequently, after incubation, the cells were subjected to trypsinization, collected, and kept in ice-cold 60 % ethanol at 4 °C for 1 h. The cells were then washed twice with 1× PBS. Subsequent to the washing procedures, the cells were treated with 100 μL of propidium iodide (PI) solution containing RNase (Cell Signaling Technology; Boston, MA). The cells were incubated for 15 min in darkness and then washed twice with 1× PBS. Flow cytometric analysis was performed on a Cytek Northern Lights (NL−2000) spectral flow cytometer (Cytek Biosciences, Bethesda, MD) with SpectroFlo Software version 2.2.0.3.

2.9. Apoptosis/necrosis analysis

A549, MCF-7, SKOV-3, and Ea-yh926 cells (1 × 10^5) were grown in

Table 1
In vitro cytotoxicity activity (IC50, μM) of dihydropyridine-sulfonamide derivatives (A1-A7) and reference compounds (AG, AG-CHO) against EA.hy926, A549, MCF-7, and SKOV-3 cancer cell lines

Code	EA.yh926	A549	MCF-7	SKOV-3
A1	35.0866 ± 6.2900	6.5216 ± 1.1824	3.7656 ± 0.5407	1.3219 ± 0.3303
A2	52.3 ± 4.4486	22.03 ± 1.6488	5.5106 ± 1.5654	7.0996 ± 2.0135
A3	52.9733 ± 6.9682	41.44	1.7806 ± 0.4250	7.7946 ± 1.9848
A4	15.3866 ± 5.2158	7.044 ± 1.5074	10.1296 ± 2.3062	33.5633 ± 5.9216
A5	1.303 ± 0.4355	16.7833 ± 2.4820	43.2933 ± 6.3400	37.17 ± 3.9214
A6	0.0692 ± 0.0068	9.5023 ± 1.7958	33.3433 ± 10.5108	31.7833 ± 4.1614
A7	82.6466 ± 25.4486	13.8133 ± 1.0774	13.2433 ± 1.7960	15.8433 ± 4.1216
AG	145.9666 ± 32.4594	49.7533 ± 29.7362	183.0666 ± 30.4592	90.9266 ± 4.5651
AG-CHO	3.4326 ± 0.3102	1.5783 ± 1.0781	1.9716 ± 0.4475	0.9277 ± 0.0771
Doxorubicin	1.96 ± 0.05	1.9 ± 0.11	1.5 ± 0.11	1.8 ± 0.044

a 6-well plate and incubated for 24 h at 37 °C. The grown cells were subsequently subjected to established IC50 doses of the synthesized DHP sulfamide compounds AG-CHO, A1, A2, A3, A5, A6, and A7, respectively, and incubated for 48 h. The untreated cells were used as control. After treatment, the cells were trypsinized and washed twice in phosphate-buffered saline (PBS). Assessment of apoptosis was carried out following the FITC Annexin V Apoptosis Detection Kit with PI (BioLegend; San Diego, U.S.A.). Cell pellets were re-suspended in 400 μL of binding buffer and stained with a mixture of 10 μL of PI and 5 μL of FITC Annexin V, and reference groups were made including unstained cells, cells with PI only, and cells used only with Annexin V-FITC. The staining was carried out by gentle mixing for 15 min at room temperature without illumination. Cellular apoptosis and necrosis was evaluated using a Cytek Northern Lights (NL-2000) spectral flow cytometer and was run with SpectroFlo Software version 2.2.0.3.

2.10. Cell autophagy assay

A549, MCF-7, SKOV-3, and Ea-yh926 cells were cultured in 6-well plates, and treated with the calculated IC50 values of the produced DHP sulfamide compounds (AG-CHO, A1, A2, A3, A5, A6, and A7). Following 48 h of treatment, the cells were washed twice with PBS and subsequently treated with 1 μg/mL of acridine orange, dissolved in PBS, for 15 min at 37 °C in a dark environment. Acridine orange is a dye that specifically marks acidic vesicular organelles (AVOs), which indicate autophagic activity. The cells were stained by incubating them with the dye, and then washed to remove surplus dye. The stained cells were then analyzed on a Cytek Northern Lights (NL-2000) spectral flow cytometer connected to SpectroFlo Software version 2.2.0.3. This allowed the detection and quantification of AVOs, thus allowing the assessment of autophagic activity in the A549, MCF-7, SKOV-3, and Ea-yh926 cell lines after treatment with produced DHP sulfamide compounds.

2.11. Statistical assay

The data were reported as the mean of these triplicates ± standard deviation (SD). In the statistical analyses, differences between control and samples were compared by the student's *t*-test. The necessary analysis was completed using GraphPad Prism 9.0 software (GraphPad, San Diego, CA, USA). A *p*-value of less than 0.05 was considered a statistically significant result. Statistical significance is indicated as * $P < 0.01$, *** $P < 0.001$, **** $P < 0.0001$. There was a total of three separate experiments conducted for each possible outcome.

3. Results and discussion

3.1. Anti-cancer activity

EA.hy926 (endothelial), A549 (lung), MCF-7 (breast), and SKOV-3 (ovarian). The panel presented a distinct difference in potency, as observed in Table 1. (Supplimentary materials S38), indicating structural characteristics differentials between the analogs. Compound A1 showed strong activity against MCF-7 (3.76 μM) and SKOV-3 (1.32 μM) along with moderate effects on A549 (6.52 μM), demonstrating its selectivity in breast and ovarian carcinoma. In contrast A3 was found to be superior breast cancer selectively effective with IC50 score of 1.78 μM when it was against MCF-7, and it still showed modest activity against SKOV-3 (7.79 μM). Conversely, A4 demonstrated potent cytotoxicity toward both lung (7.04 μM) and breast (10.12 μM) carcinoma but was substantially less effective in ovarian cancer (33.56 μM), indicating a certain cancer type specificity. Remarkably, A5 and A6 were highly potent in EA.hy926 cells (1.30 μM and 0.069 μM, respectively) suggesting the possibility that, while one might have a dual antagonism to cancer cells and anti-angiogenic, the toxicity to the endothelium contributes on the other hand to both tumor and angiogenic activities but also should be considered with caution for therapeutic work. A7 showed moderate and broad-spectrum activity without strong selectivity. AG (parent drug) showed weak cytotoxicity in all the cell lines (50–183 μM) compared with the reference compound counterparts, indicating that structural modification increased activity. AG-CHO showed the greatest and uniform activity across all models (0.92–3.43 μM) and served as the best experimental efficacy standard for anticancer therapy, the efficacy results were also compared with Doxorubicin as a standard drug, as shown in Table 1.

Overall, the SAR trends highlight that A1 and A3 are promising for breast and ovarian cancer, A4 for lung and breast cancer, while A5 and A6 show strong endothelial inhibition with potential antiangiogenic relevance. The results complement the molecular dynamic findings, where A4 demonstrate superior stability and residue-specific interactions with AKT1 compared to A1.

3.2. Apoptosis

The Annexin V-FITC/PI flow cytometry results demonstrate that the tested compounds induced apoptosis in cancer cells (SKOV-3, MCF-7, and A549) while exerting minimal cytotoxicity on normal endothelial cells (EA.HY.926). In A549 cells, AG-CHO and test compounds markedly increased apoptotic populations, with A1 inducing the highest combined early and late apoptosis, while A4 preserved a larger proportion of live cells see Fig. 1A. In contrast, EA.HY.926 cells maintained high viability across treatments, especially with A4, confirming selective toxicity toward cancer cells (Fig. 1B). In SKOV-3 cells, AG-CHO and compounds A1-A3 significantly reduced viability with A3 showing the strongest effect by increasing late apoptosis, (Fig. 2A) whereas MCF-7 cells were highly sensitive to A2, which predominantly triggered early apoptosis, and A3 promoted late apoptosis (Fig. 2B).Collectively, these findings indicate that compounds exert anticancer effects through apoptosis induction, with varying potency across different cancer cell lines, while sparing normal cells, highlighting their potential as selective anticancer agents.

3.3. Cell cycle

Cell cycle distribution analysis was performed using flow cytometry to investigate the effect of the tested compounds (A1-A7) and AG-CHO on different cancer (SKOV-3, MCF-7, A549) and endothelial (EA.HY.926) cell lines. In untreated control groups, cells showed a normal distribution across G1, S, and G2 phases. Treatments with compounds had a pronounced effect on this balance, signifying that compounds could arrest cells in certain stages of the cell cycle and thereby prevent

cell proliferation. Treatment of SKOV-3 cells as shown in Fig. 3A and treatment with AG-CHO showed significant differences in cell differentiation and cell proliferation when tested against control. It is noteworthy that compound A2 induced intense G1 phase arrest; >70 % of cells were sequestered in this phase and compound A3 induced a strong S-phase enrichment. These results imply that A2 and A3 inhibit DNA synthesis or DNA replication in two distinct ways to suppress proliferation. For MCF-7, compound A1 and A2 were the most efficient at triggering S-phase arrest, while AG-CHO also directed cells to G2 accumulation. This would support that the compounds inhibit DNA replication for breast cancer cells probably through the inhibition of cell cycle regulatory proteins involved in replication and control of checkpoints. EA.HY.926 endothelial cells (Fig. 4A), A6 and A7 showed high levels of activity, A6 resulted in significant G1 arrest while A7 shifted most of the cells to S phase. Both compounds substantially inhibited progression into G2/M phase relative to controls, which might explain the anti-angiogenic effect of both compounds via suppression of the endothelial reproduction. AG-CHO induced a robust G1 arrest in A549 lung cancer cells (Fig. 4B) while compound A1 also induced G1 cell cycle blockade. In contrast, compound A7 caused accumulation of S phase, which correlates with that in endothelial cells.

Compounds exhibit diverse but significant effects on cancer cell cycle progression. The ability of A2 (SKOV-3), A1/A2 (MCF-7), A6(EA.HY.926), and A1/A7 (A549) to induce G1 or S arrest strongly support their potential as therapeutic agents.

3.4. Flow cytometry analysis (autophage)

Flow cytometry analysis of acridine orange-stained cells demonstrated a significant induction of autophagy (AVOs) across different cancer cell lines (SKOV-3, MCF-7, A549) and endothelial-derived EA.hy926 cells following treatment with AG-CHO and its derivatives (A1–A7). In SKOV-3 cells (Fig. 5A), AG-CHO and A1 notably enhanced autophagy compared with the control, while A2 and A3 induced relatively lower levels, suggesting variable potency among derivatives. In MCF-7 cells (Fig. 4B), AG-CHO strongly upregulated autophagic

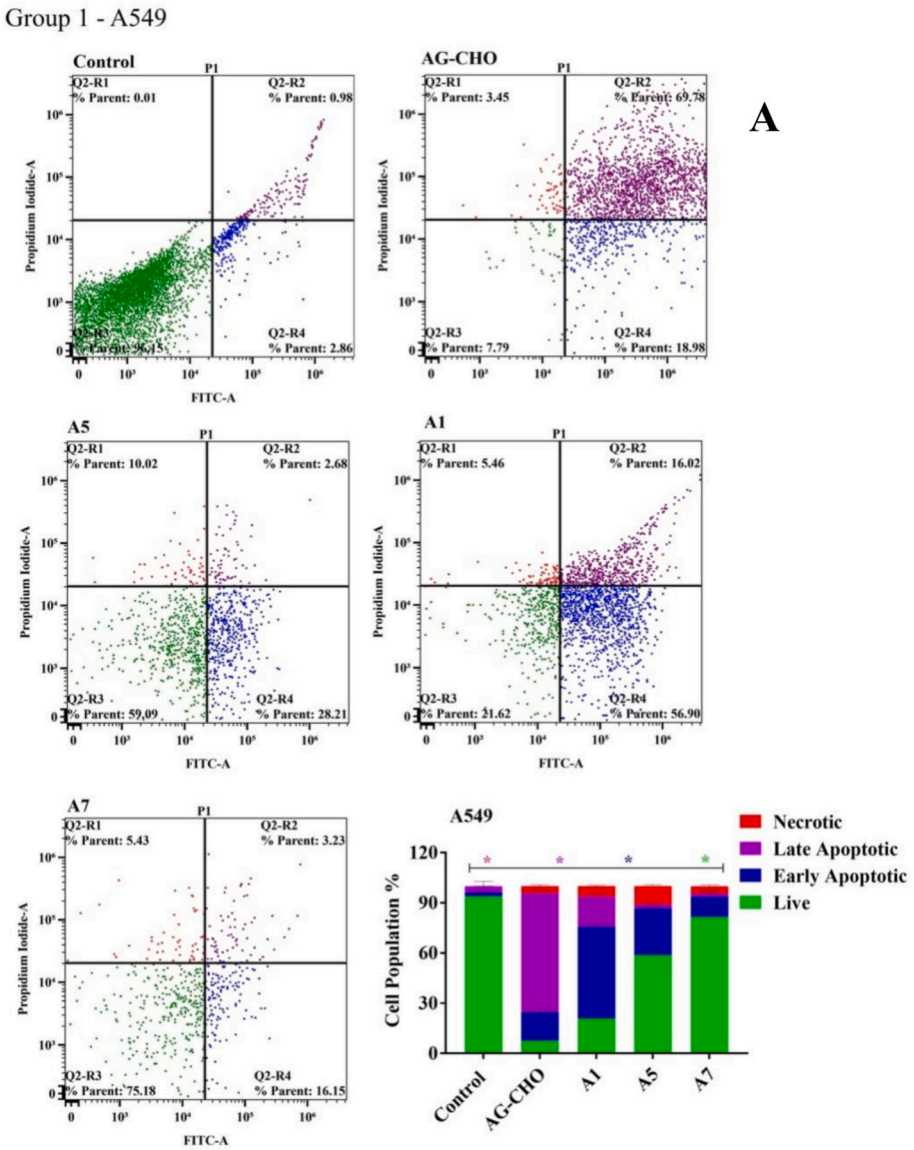

Fig. 1. Flow Cytometry analysis of apoptosis in (**A**) A549, (**B**) EA.HY.926 cells following treatment with AG-CHO and test compounds (A1 and A7). Cells were stained with Annexin V-FITC/PI to distinguish live (green, lower-left), early apoptotic (blue, lower-right) late apoptotic (purple, upper-right), and necrotic (red, upper-left) populations. Bar graphs summarize percentage cell populations. (For interpretation of the references to colour in this figure legend, the reader is referred to the web version of this article.)

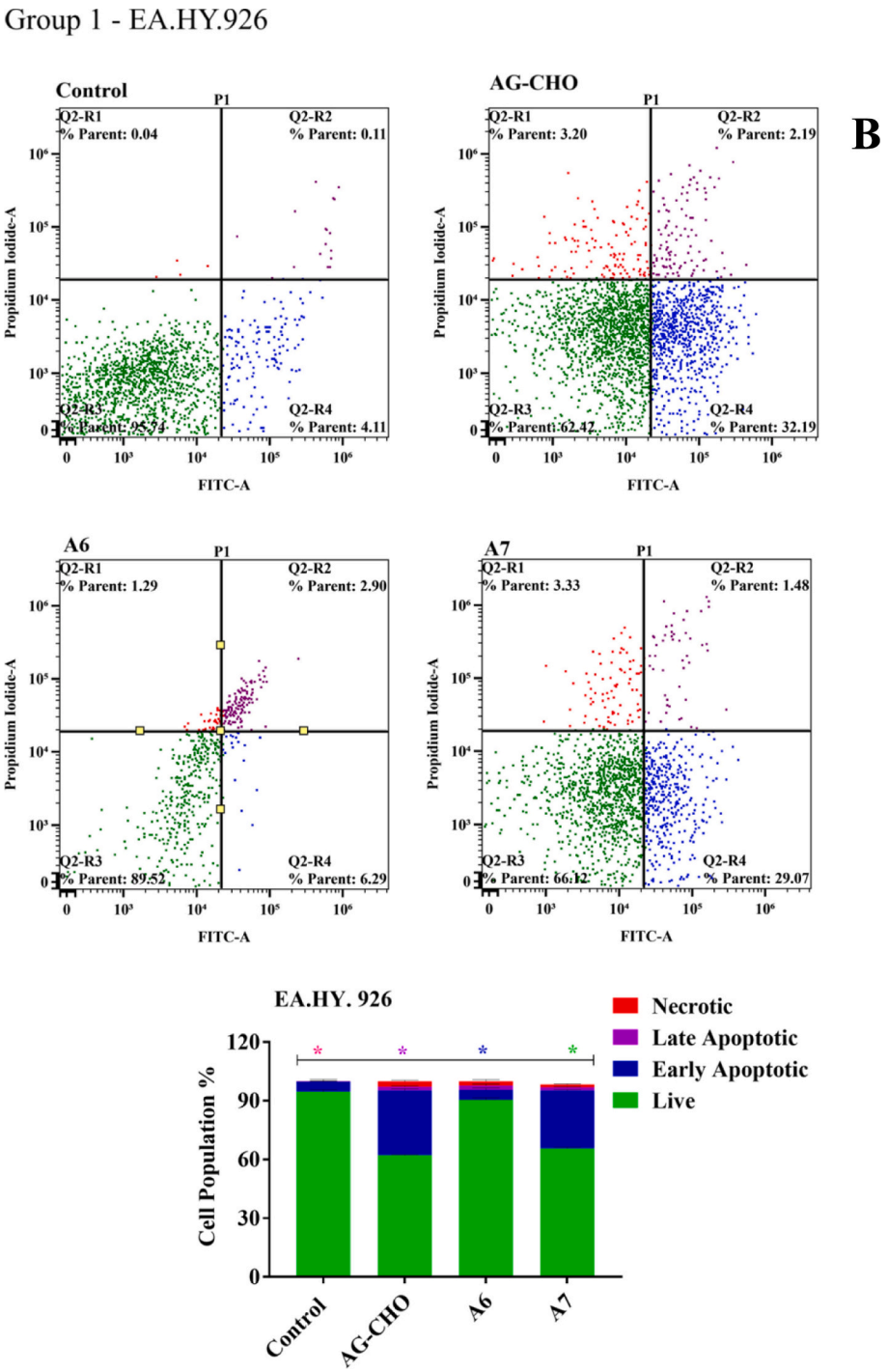

Fig. 1. (*continued*).

vacuoles compared to control, whereas A1–A3 induced moderate effects, indicating that the parent compound has superior activity in this cell line. In EA.hy.926 cells (Fig. 6A), both A6 and A7 markedly increased autophagy beyond the effect of AG-CHO, highlighting their potential as more effective inducers of autophagy in endothelial cells. Similarly, in A549 cells (Fig. 6B), AG-CHO triggered a robust autophagic response, while derivatives A1, A5, and A7 also showed significant but comparatively moderate activity. Quantitative bar graphs confirm statistically significant increase in autophagic cell percentages across treated groups compared with control (* $P < 0.05$, ** <0.01, *** <0.001), with notable variation in response depending on both the compound and cell line. Collectively, these findings indicate that AG-CHO consistently induces autophagy in all tested cell lines, while its derivatives display cell-type specific differences in efficacy, suggesting potential for selective therapeutic targeting.

3.5. Pharmacology network analysis

The compound-target network showed that the compounds which were studied have multiple interactions with proteins and this reflects the multi-target pharmacological potency of the compounds considered (Fig. 7). This network constituted the base of predicted targets for downstream studies. To add clarity to these insights into the context of diseases, a compound-disease-target interaction network was formed

(Fig. 8), revealing that compounds target similar proteins associated with diseases. These common targets are the molecular candidates to target therapeutically. A protein-protein interaction (PPI) network was formed to evaluate the biological significance of these overlapping targets (Fig. 9). The discovery of several highly interconnected hub nodes indicates their essential role in regulating disease pathways. Protein-protein interaction (PPI) analysis of these overlapping proteins shows a densely connected network of several backbone proteins, among which AKT1, SRC, TNF, STAT3, and EGFR stood out as the most interlinked nodes, suggestive of their location at the hub of chemical-molded networks. These proteins all participate in major signaling pathways that steer inflammation, cell growth, programmed cell death, and metabolism. So far, among these nodes AKT1 has been identified as one of the most interconnected proteins with all its potential roles as a core member of regulatory molecules.

Finally, topological analysis was performed to rank the targets according to network parameters, including degree, betweenness, and closeness centralities. The top ranked gene graph (Fig. 10) confirmed AKT1 as one of the leading hub genes, consistently emerging at the highest rank compared to other candidates. Taken together, these results strongly support AKT1 as the most rational therapeutic target, integrating evidence from compound-target predictions, disease relevance, network centrality, and topological ranking.

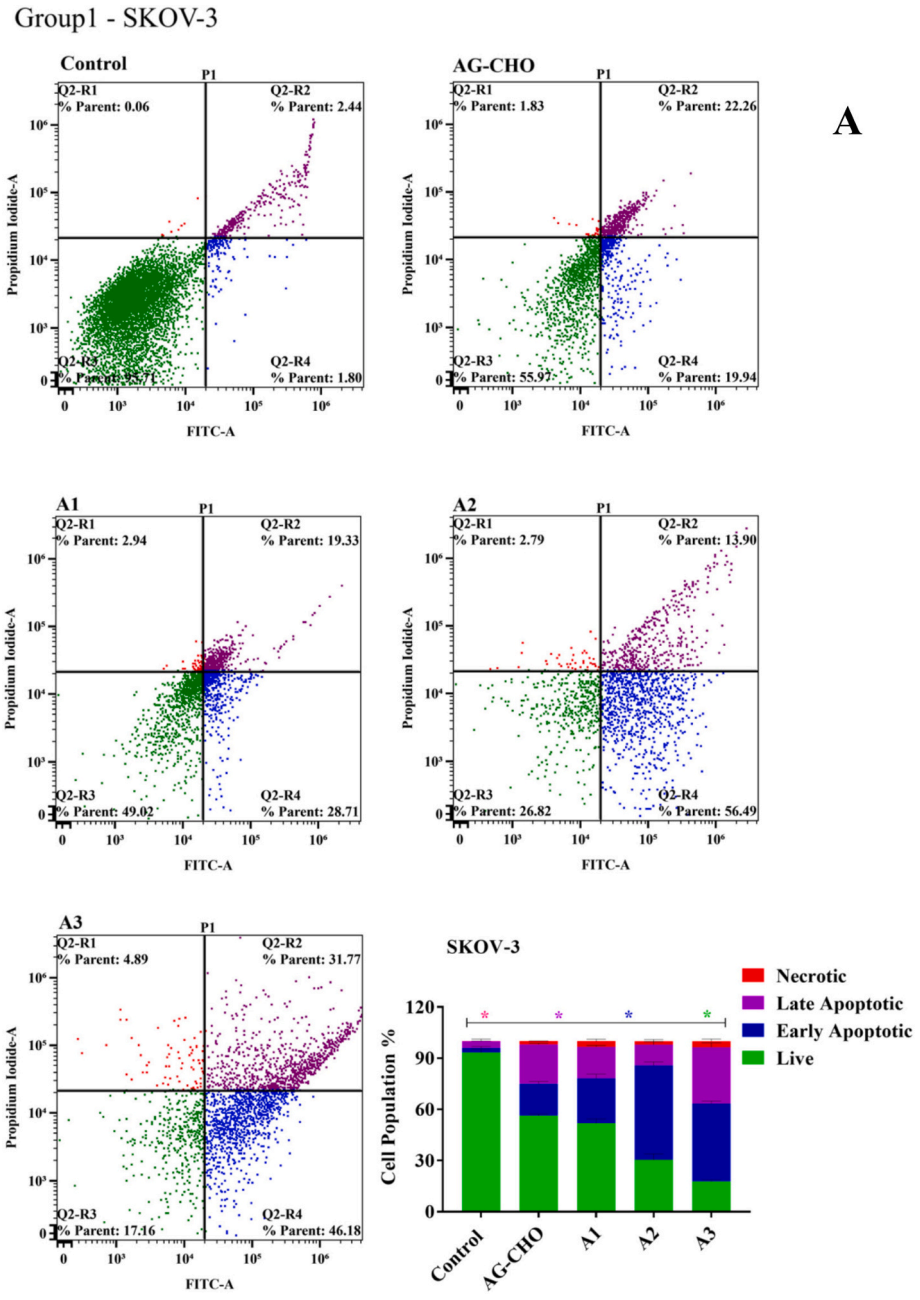

Fig. 2. Flow Cytometry analysis of apoptosis in (**A**) SKOV-3, (**B**) MCF-7 cells following treatment with AG-CHO and test compounds (A1–A7). Cells were stained with Annexin V-FITC/PI to distinguish live (green, lower-left), early apoptotic (blue, lower-right) late apoptotic (purple, upper-right), and necrotic (red, upper-left) populations. Bar graphs summarize percentage cell populations. (For interpretation of the references to colour in this figure legend, the reader is referred to the web version of this article.)

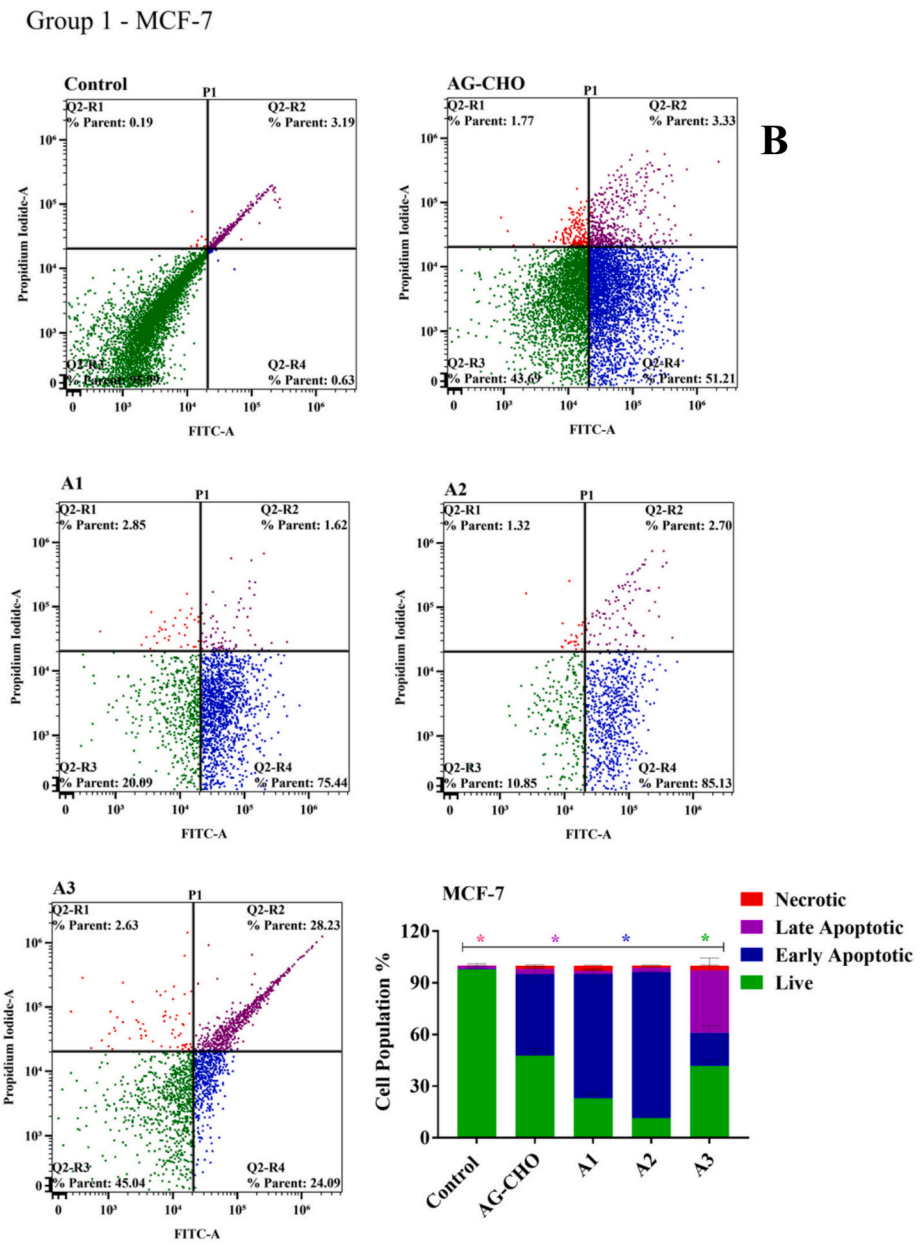

Fig. 2. (*continued*).

3.6. ADMET study results

The comparative analysis of the six molecules as indicated in Table 2 reveals several key trends in their physicochemical, pharmacokinetic, and drug likeness properties, with most compounds- including molecule 5 facing significant challenges for drug development, especially for oral bioavailability.

All six molecules have high molecular weights (>540 g/mol), violating Lipinsk's rule, which recommends MW < 500 for good oral bioavailability. They also all have 10 rotatable bonds, indicating high molecular flexibility, which generally reduces bioavailability and target selectivity. These parameters contribute directly to their Lipinski violations (2 each) and lead-likeness violations, primarily due to MW > 350 and rotatable bonds >7. Hydrogen bond donors and acceptors are consistent across the set, with 2 donors and 8–9 acceptors, maintaining reasonable balance. However, topological polar surface area (TPSA) values are all above 160 $Å^2$, and in the case of molecule A2 (192.19 $Å^2$) exceeds Egan's and Veber's rules for good membrane permeability. Among the analyzed compounds, molecule A5 has the lowest TPSA (163.95 $Å^2$), suggesting marginally better membrane permeability relative to the others. In general, the high TPSA values observed across the series largely explain their poor gastrointestinal (GI) absorption predictions. Lipophilicity values expressed as the ILOGP-predicted LOGP (octanol/water) are moderate (3.0–3.4) for most molecules, with molecule A7 displaying the lowest (2.37), potentially improving solubility but diminishing permeability. Consistently, aqueous solubility (log S, ESOL) is low (−5.52 to −6.02) for most compounds, except A7 (−4.96), which shows comparatively higher solubility. Consequently, A7 appears slightly more suitable for oral administration, albeit still suboptimal. All compounds are predicted to have low GI absorption, no blood-brain barrier permeability, and are not substrates for P-glycoprotein, which may help prevent efflux-mediated resistance.

However, all are inhibitors of CYP2C9 and CYP3A4, two key enzymes in drug metabolism, this presents a major risk of drug-drug interactions. Notably, molecule A3 also inhibits CYP1A2 and CYP2C19, in addition to the major isoforms CYP2C9 and CYP3A4, thereby

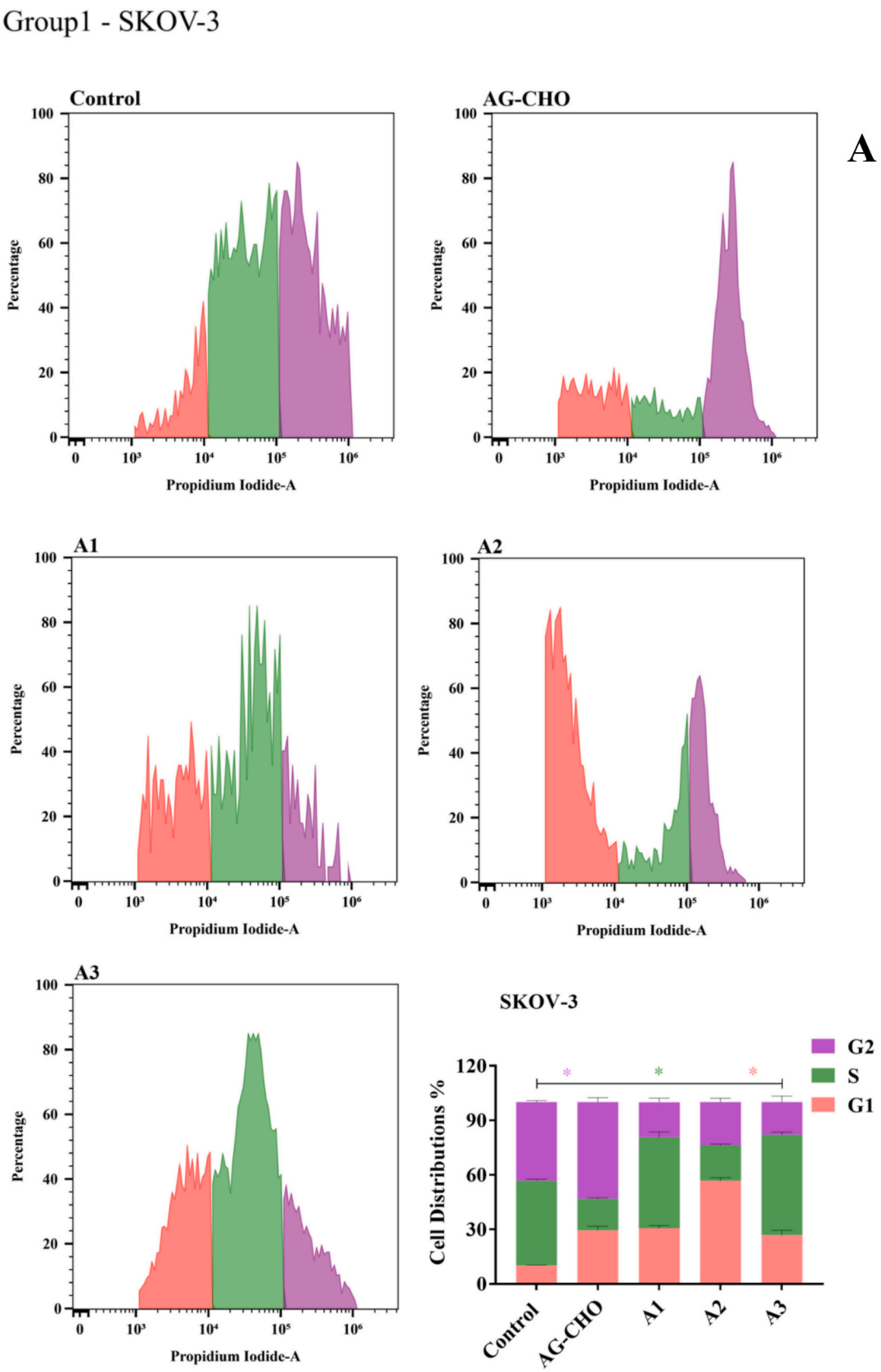

Fig. 3. Cell cycle analysis of A; SKOV-3 ovarian cancer cells following treatment with AG-CHO and compounds A1–A3. B; MCF-7 breast cancer cells after exposure to AG-CHO and compound A1–A3. Histogram show the proportion of cells in G1 (red), S (green), and G2/M (purple) phases. The bar graph summarizes cell cycle distribution percentages. (For interpretation of the references to colour in this figure legend, the reader is referred to the web version of this article.)

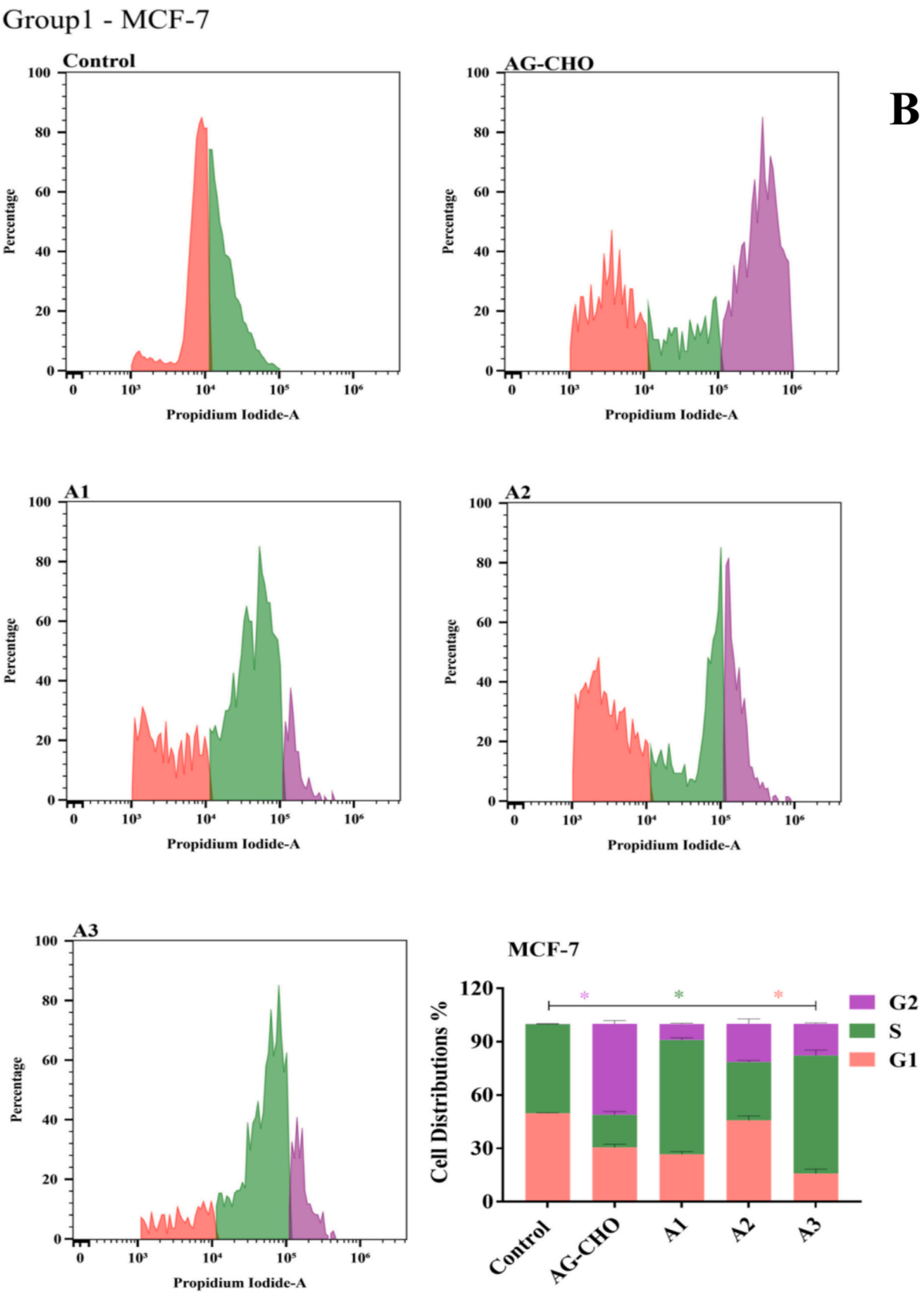

Fig. 3. (*continued*).

representing the highest metabolic risk among the studied compounds. All molecules violate two of Lipinski's rule, primarily due to their high molecular weight and flexibility, and exhibit a low bioavailability score (0.17), consistent with their predicted poor absorption. Synthetic accessibility scores are fairly uniform (4.9–5.0), reflecting moderate to high synthetic complexity. Among them, molecule A7 shows the lowest

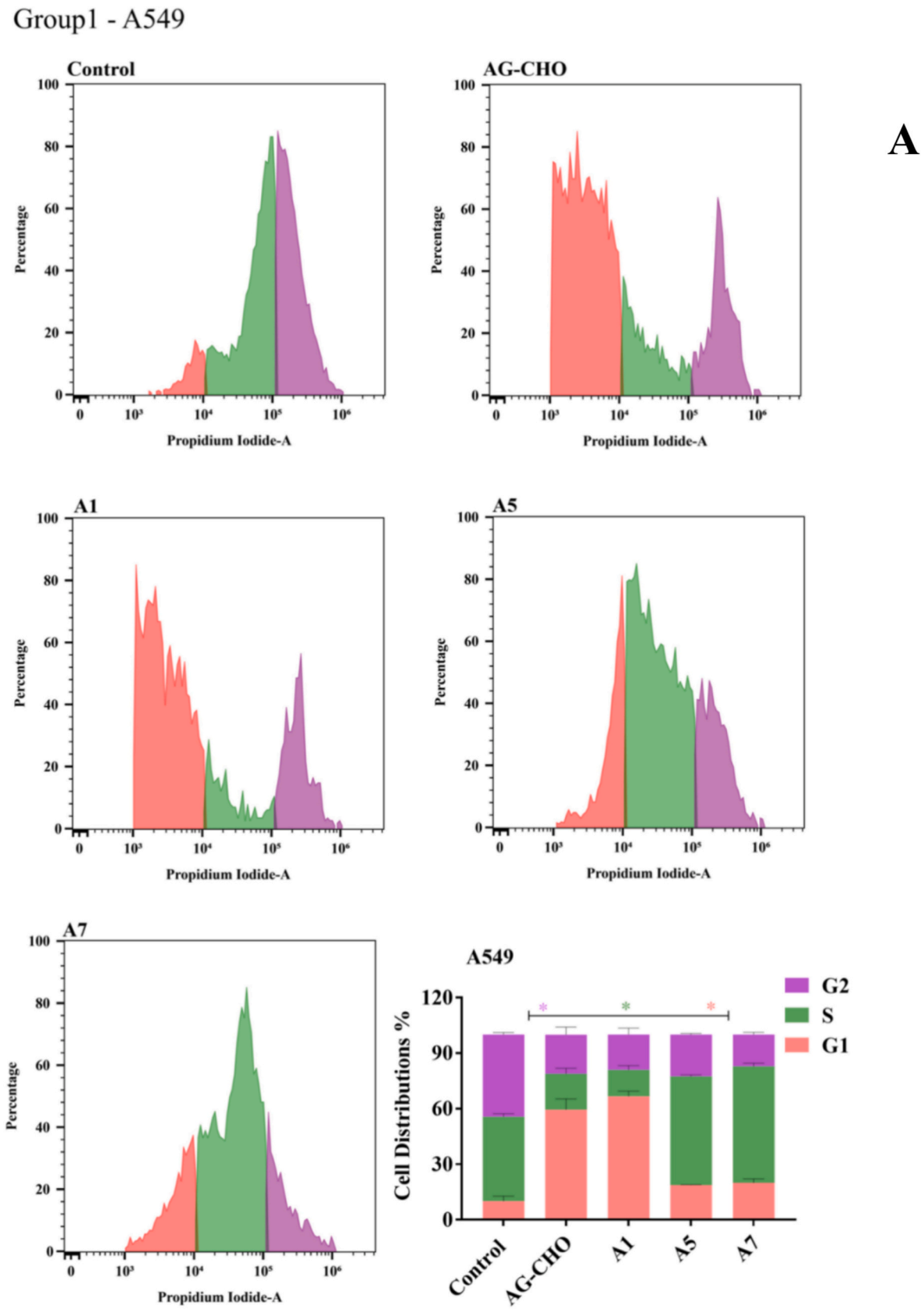

Fig. 4. Cell cycle analysis A; Cell cycle effects of AG-CHO and compounds A1, A5 and A7 on A549 lung cancer cells. B; Cell cycle profiles of EA.HY.926 endothelial cells treated with AG-CHO and Compounds A6–A7. Histogram show the proportion of cells in G1 (red), S (green), and G2/M (purple) phases. The bar graph summarizes cell cycle distribution percentages.

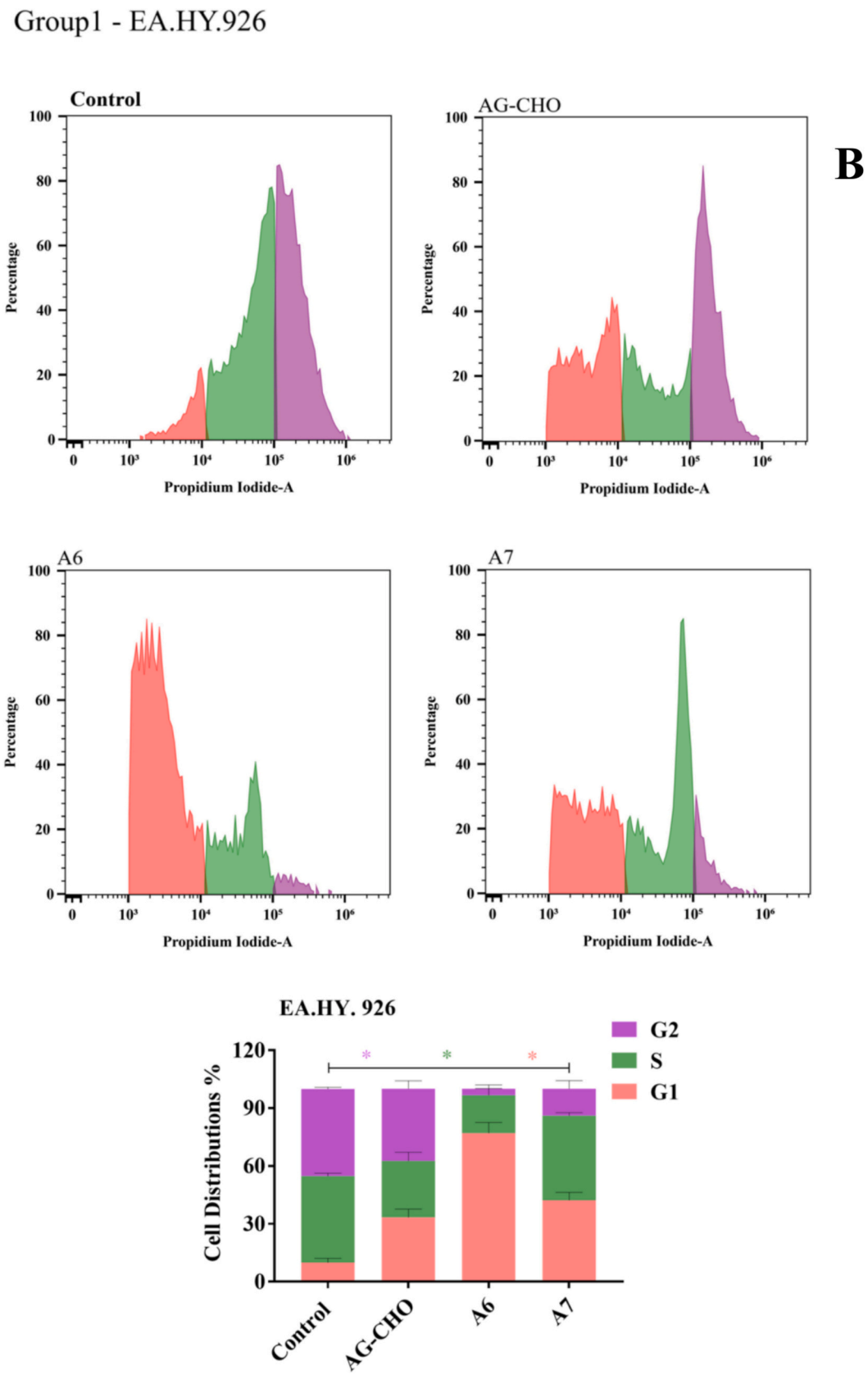

Fig. 4. (*continued*).

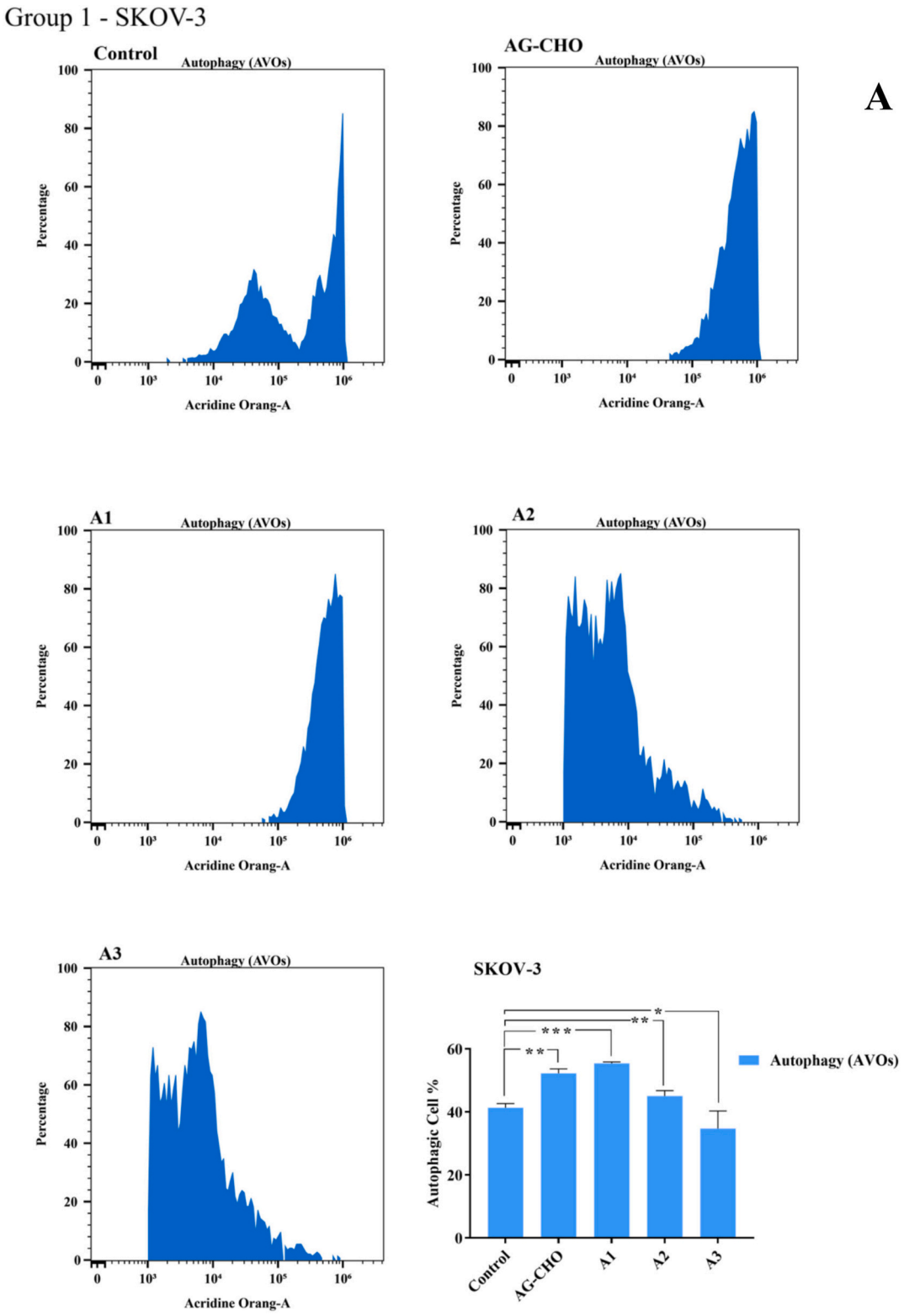

Fig. 5. Flow cytometry analysis of autophagy (AVOs) in (A) SKOV-3 cells (B) MCF-7 cells stained with acridine orange after treatment with AG-CHO and derivatives (A1-A3). Histograms show distribution shifts compared to control, with quantitative bar graph summarizing percentage of autophagic cells. Data represent mean ± SD; *$p < 0.05$, **$p < 0.01$, *** $p < 0.001$.

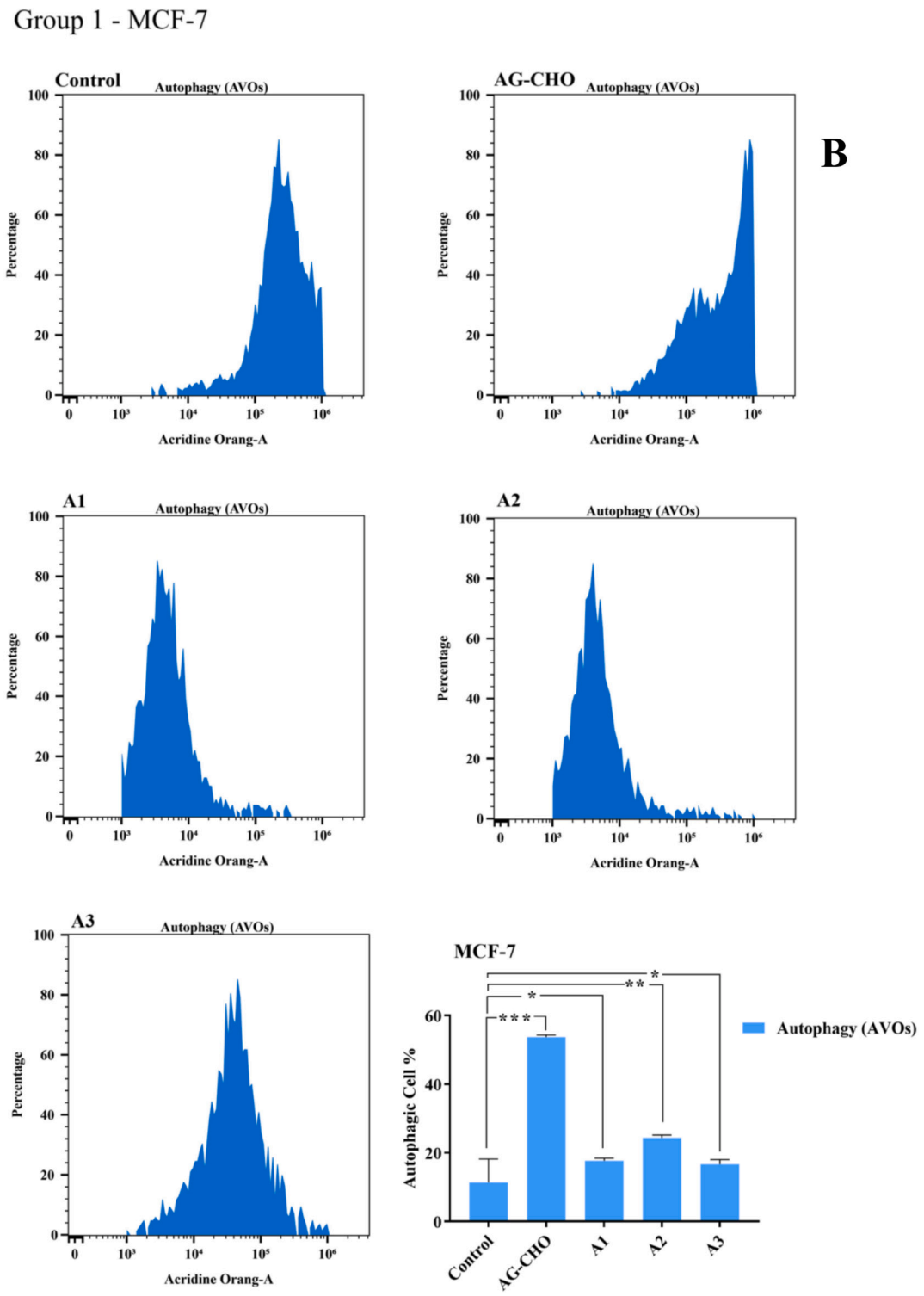

Fig. 5. (*continued*).

score (4.79), suggesting it is slightly easier to synthesize.

3.7. Molecular docking

The docking analysis of the candidates compounds against AKT1 are listed in Table 3 according to docking scores that ranging from −5.4 to 6.8 kcal/mol, with more negative values indicating stronger predicted binding affinity. The most favorable scores were observed for A1 and A4 (−6.8 kcal/mol), followed closely by A6 (−6.5 kcal/mol) and A3 (−6.4 kcal/mol). Weaker binding was predicted for AG (−5.4 kcal/mol) and AG-CHO (−5.7 Kcal/mol). Interaction profiling showed that A1 and A4 both formed hydrogen bonds with Ile19, a key residue in the AKT1 active site [36,37]. Notably, A1 achieved a shorter bond distance (1.86 A°) compared to A4 (3.8 A°), suggesting a stronger and more geometrically favorable interaction profile despite their identical docking score. A2, A3 and A5 acted on Arg23, though the longer H-bond distances (3.87–4.05 A°) may minimize this activity. A5 was activated for ASP108 with the bond length of 3.51 A° suggesting that it could be an alternative

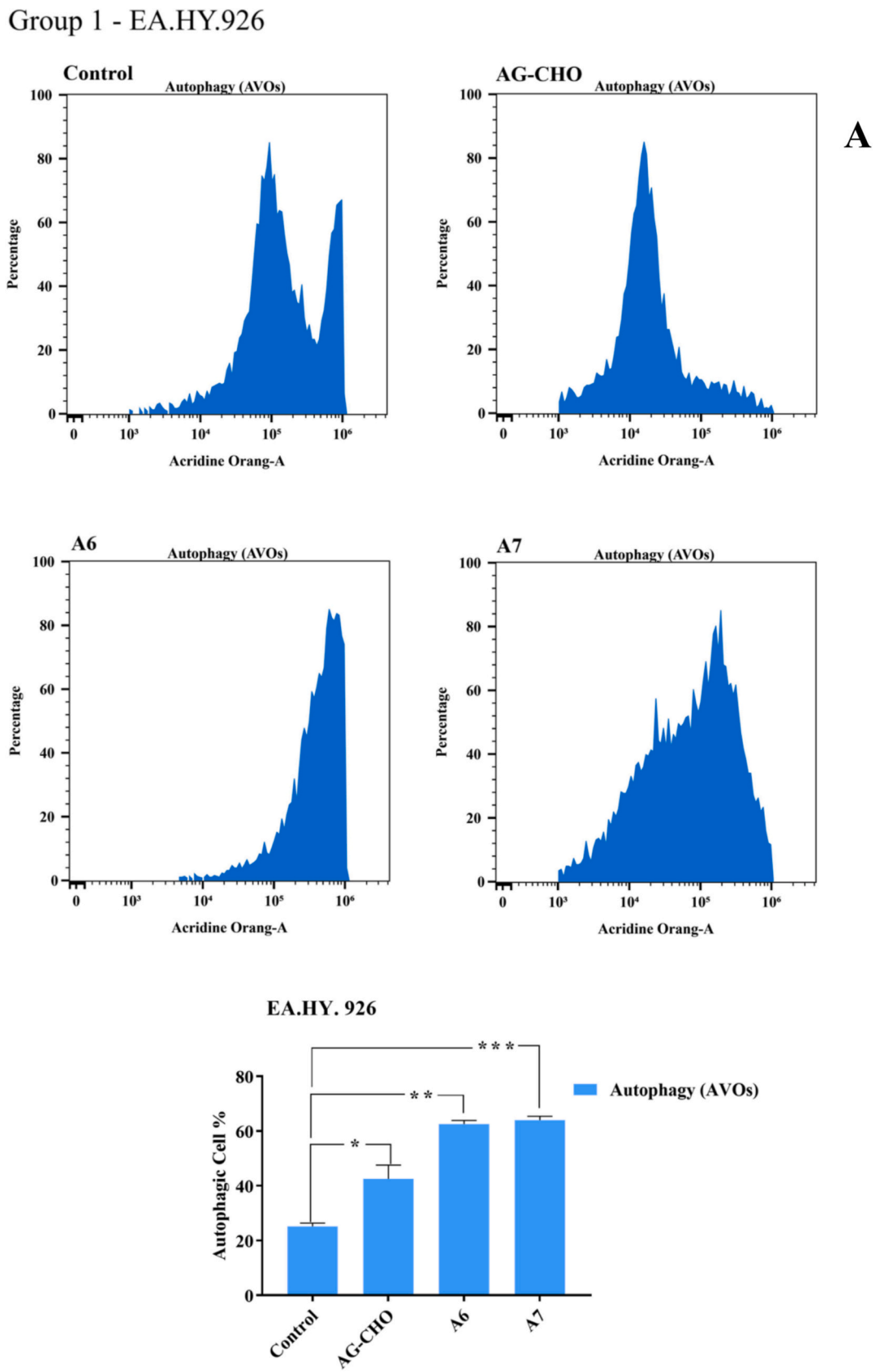

Fig. 6. Flow cytometry analysis of autophagy (AVOs) in (A) EA.hy.926 cells (B) A549 cells stained with acridine orange after treatment with AG-CHO and derivatives (A1-A3). Histograms show distribution shifts compared to control, with quantitative bar graph summarizing percentage of autophagic cells. Data represent mean ± SD; *$p < 0.05$, **$p < 0.01$, *** $p < 0.001$.

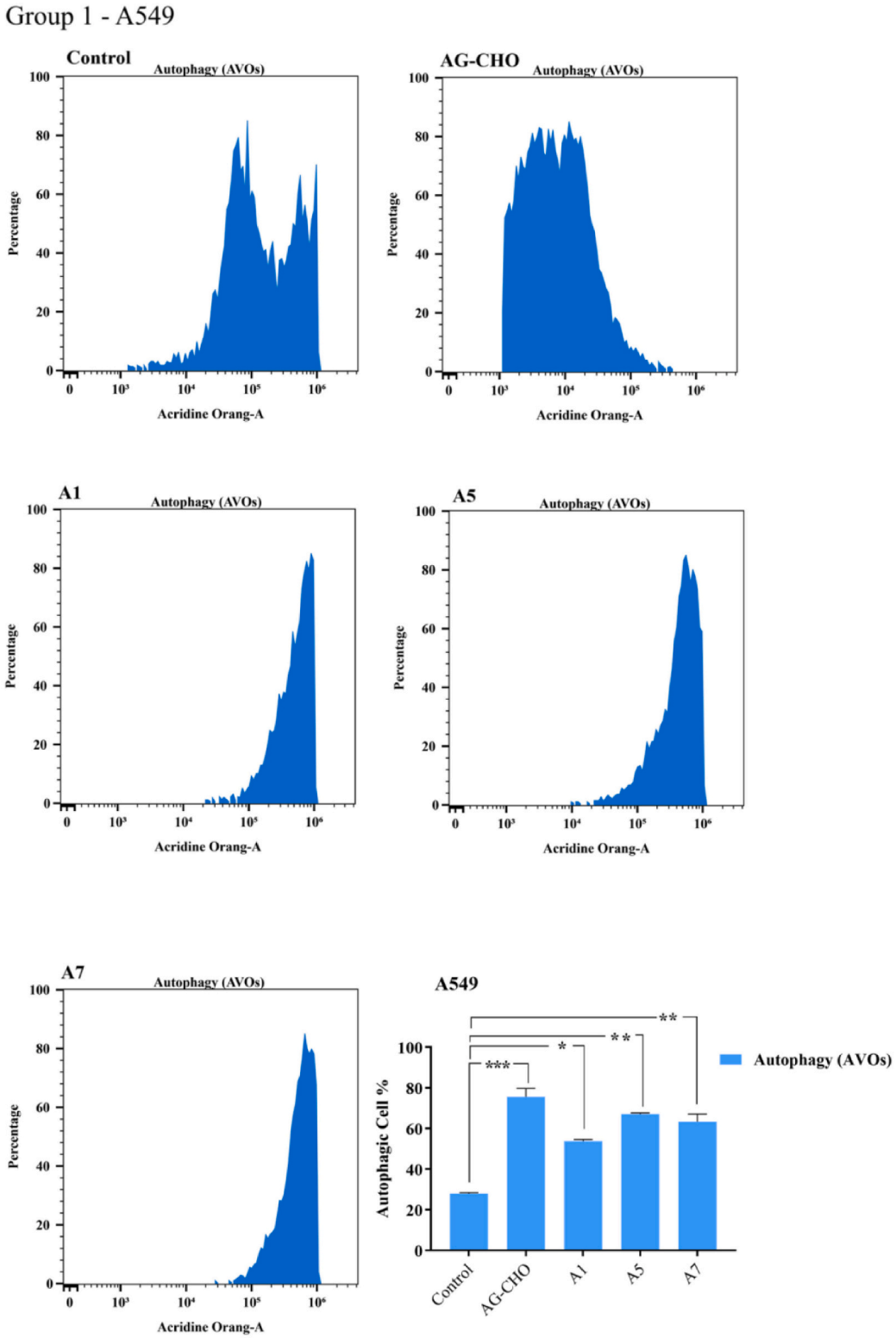

Fig. 6. (*continued*).

binding method that might affect binding diversity, and A6 did so with Lys20 (3.84 A°) and AG-CHO with Lys39 at the longest measured bond distance of 4.92 A°. These data indicate that the ligands Ile19 and Arg23 were the major binding sites within the AKT1 binding pocket, and compounds targeting those elements at optimal bond lengths had better docking results. Referring to both docking affinity and interaction geometry, A1 is the candidate at the highest efficiency as see Fig. 11, A4 (Fig. 12) and A5 are preferred ones, as they pair strong predicted binding for the binding reaction with favorable engagement of the residues.

3.8. Molecular dynamic studies

The AKT1 protein in complex with ligands A1 and A5 was subjected to molecular dynamics (MD) simulation for 100 ns to examine the

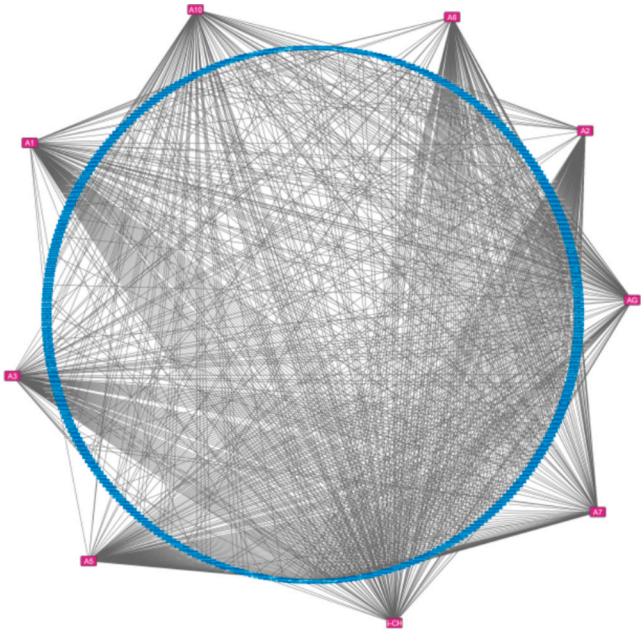

Fig. 7. compound -target network; A circular network showing the interaction between active compounds (pink nodes on the periphery) and their predicted target genes (blue nodes). the dense interactions highlight the multitarget nature of the compounds.

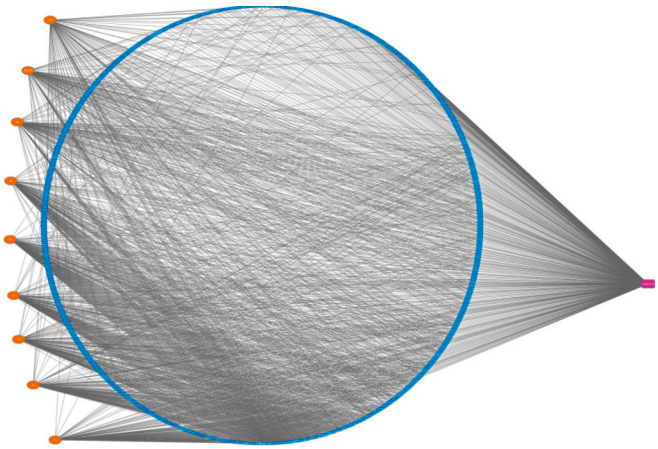

Fig. 8. Compound -Disease-Target Interaction Network; a network representation linking bioactive compounds (orange node), disease-associated targets (purple nodes) and the overlapping shared targets (blue nodes). (For interpretation of the references to colour in this figure legend, the reader is referred to the web version of this article.)

stability of binding interaction and dynamics under the same NPT conditions (310 K, 1 atm). The analyses were based on root mean square deviation (RMSD) and root mean square fluctuation (RMSF) in addition to secondary structure stability, protein-ligand interactions, ligand flexibility, and conformational torsion profiles. The comparative results give evidence for the different stability and interaction profiles of these two ligands [38].

3.8.1. *Structural stability (RMSD)*

In Fig. 13 (A and C), both the protein RMSD of AKT-A1 and AKT-A5 complexes stabilized, oscillating around a limit value of 1–3 Å, providing evidence of well-equilibrated and stable protein backbones in both systems. The AKT1-A1 complex settled marginally earlier and had lower changes (~1.8–2.2 Å) than that of AKT1-A5 (~2.0–2.6 Å), indicating an increased conformational stability of the A1-targeted system. Ligand RMSD values were also always lower than 2.5 Å for A1 and confirmed that the protein binding position in the binding pocket was stable, and while A5 had slightly higher ligand RMSD values (~2.8 Å), indicating that the ligand might change the position slightly during the trajectory.

3.8.2. *Residual flexibility (RMSF)*

Residue-wise RMSF profiles for both complexes, shown in Fig. 13 (B and D), revealed comparable flexibility trends, with higher fluctuations localized at the N-and C-terminal regions and loop segments, as expected for AKT1. Whereas residues directly involved in ligand binding remained relatively rigid. Interestingly, slightly lower RMSF values were observed for ligand-contact residues in the A5 complex, suggesting that A5 may contribute to greater local structural rigidity, possibly due to its broader interaction coverage within the binding pocket, which maintained tighter binding-induced rigidity in key residues such as Glu17, Gln79, and Thr82.

Analysis of secondary structure element (SSE) revealed that the AKT1-A5 complex retained 53.61 % SSE content (14.02 % helices, 39.6 % strands), while AKT1-A1 showed 50.33 % SSE (12.74 % helices, 37.59 % strands). The greater retention of structure, likely due to stronger or more persistent ligand interactions (see supp Fig. 11). Protein-ligand contacts; a detailed comparison of protein-ligand contacts demonstrated that A5 formed a broader range of interactions, including hydrogen bonds, hydrophobic interactions, ionic contacts, and water bridges with key residues engaging the ligand for a longer fraction of the simulation time. The time line plots (Fig. 14A and B) and residue interaction maps (Fig. 14C and D) showed that A5 maintained more consistent multi-type contacts often involving multiple simulations interactions with same residue (e.g., ARG, ASP, GLU side chains). A1, while forming strong and stable interactions, exhibited fewer multi-type contacts and less interaction persistence overall.

Ligand flexibility and torsion profiles; the ligand RMSF (see supp Fig. 12) showed that both ligands maintained internal structural stability. However, A1 exhibited slightly lower atomic fluctuations, consistent with its lower RMSD. The torsion profile revealed that both ligands adopted low-energy conformations throughout the simulation, but A5 displayed a broader distribution of accessible torsion angles, which may explain its more adaptive binding behavior. This torsional flexibility may also allow A5 to better accommodate binding site dynamics or engage in more diverse interactions. Both ligands showed comparable molecular surface area (MolSA), solvent-accessible surface are (SASA) and polar surface area (PSA), indicating similar solvation behavior. However, A5 formed a slightly greater number of intramolecular hydrogen bonds, which could contribute to enhanced conformational stability in solution or during binding.

3.9. *Relationship studies of structure activity*

The structure-activity relationship (SAR) analysis of the synthesized dihydropyridine-sulfonamide derivatives (A1–A7) reveal that specific structural features play a pivotal role in modeulating their anticancer activity particularly through interactions with AKT1 kinase target, akey regulator of the PI3K/AKT signaling pathway involved in cancer cell survival and proliferation. The SAR indicates that three structural domains play a major role in modulating biological activity: (i): the heterocyclic pharmacophilic group, (ii): the sulfonamide linkage, and (iii) the aromatic /lipophilic moiety as indicated in Fig. 15. Compounds A1, A4, and A6, which contain electron-withdrawing substituents and heterocyclic rings, exhibited the most favorable docking scores (−6.8 to 6.2 kcal/mol) and potent cytotoxic activity, particularly against MCF-7 and SKOV-3 cell lines. The presence of electron-withdrawing substituents, notably the nitro (-NO_2) and chloro (—Cl) groups, markedly enhances the electrophilic nature of the molecules, improving their reactivity biological target and kinase active site. These groups promote

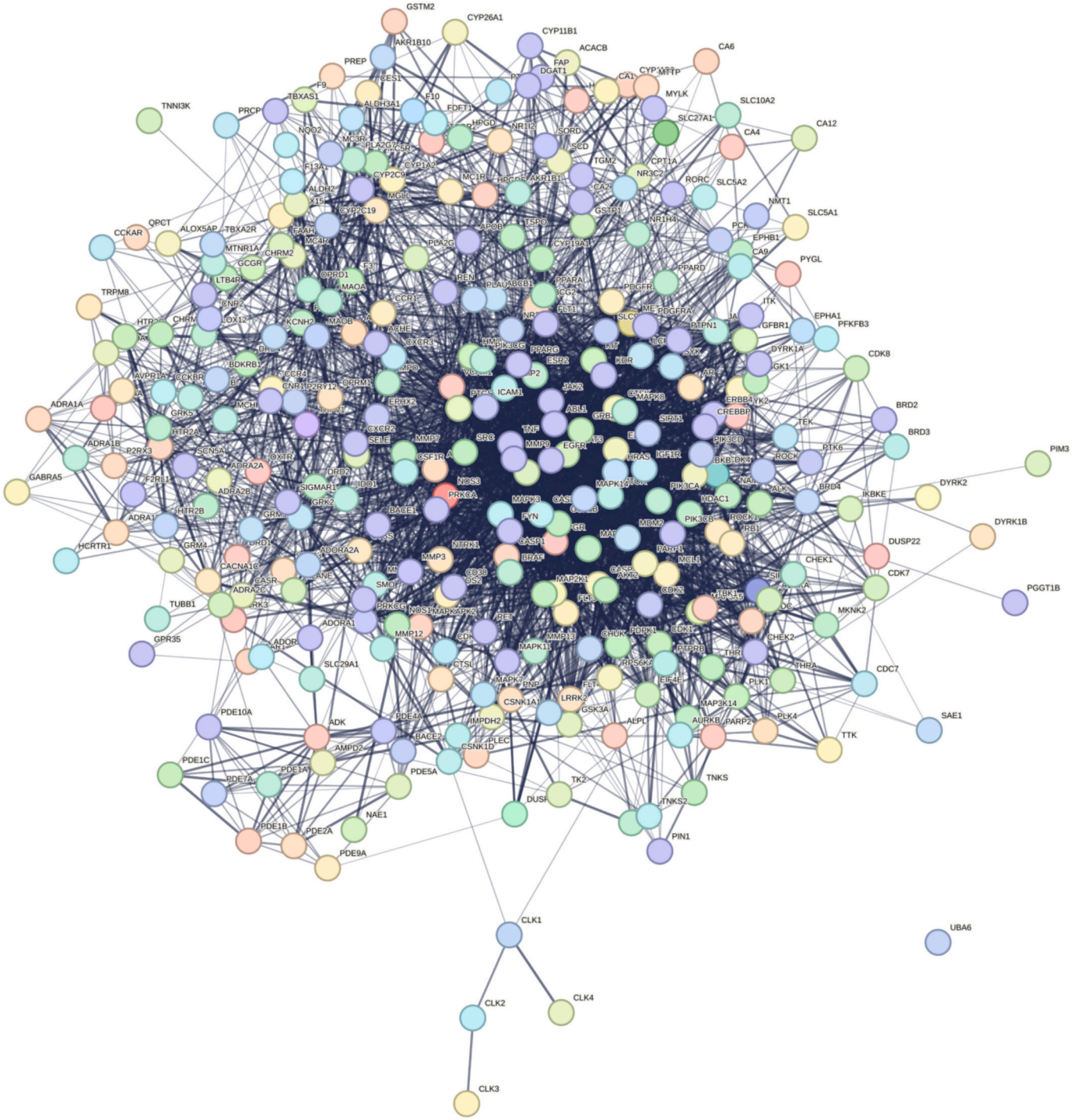

Fig. 9. Protein-Protein interaction (PPI) Network; the PPI network illustrates interactions among candidate targets. Nodes represent proteins while edges indicate interactions. Highly connected hub proteins, especially AKT1, are centrally located, highlighting their importance in key signaling pathways.

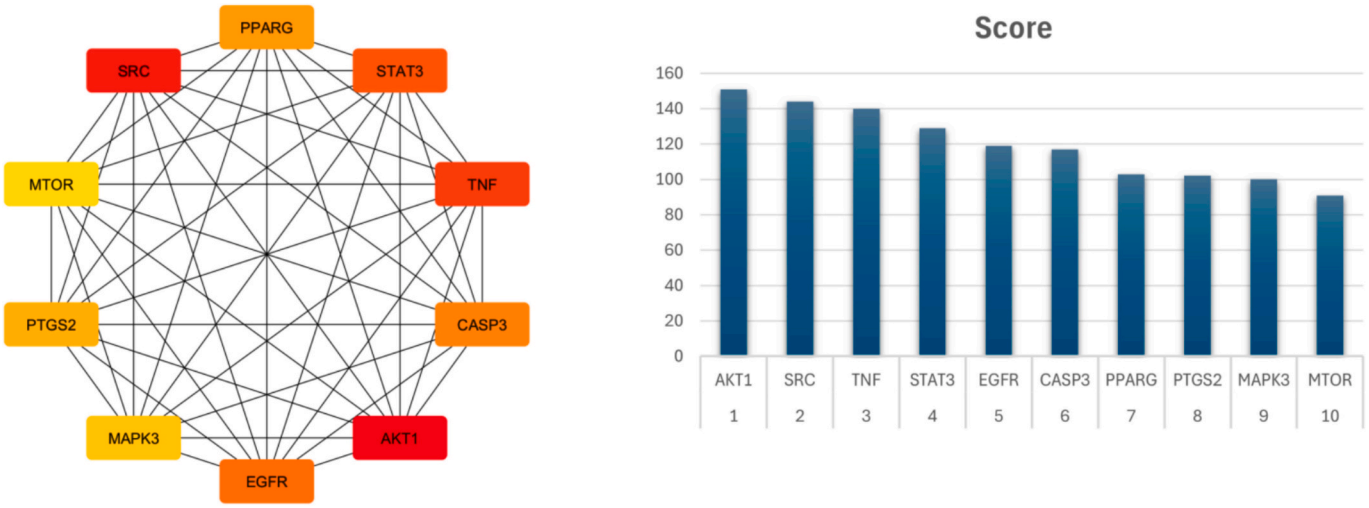

Fig. 10. Top 10 ranked target protein along with the bar chart of the top 10 hub genes ranks targets by degree centrality within the network. Genes such as AKT1, IL6, AND MAPK1 emerged as top hubs.

Table 2
ADMET profiles of compounds (A1–A7).

Parameter	Molecule A1	Molecule A2	Molecule A3	Molecule A5	Molecule A6	Molecule A7
Molecular weight (g/Mol)	586.02	588.06	583.02	582.03	597.04	546.98
Num. Rotatable bonds	10	10	10	10	10	10
Num. H-bond acceptors	9	8	9	8	9	8
Num. H-bond donors	2	2	2	2	2	2
Log Po/w (ILOGP)	3.44	3.03	3.09	3.40	3.16	2.37
Tpsa (Å2)	177.09	192.19	176.84	163.95	176.84	168.13
Log S (Esol)	−5.67	−6.02	−5.52	−5.93	−5.85	−4.96
Gi absorption	Low	Low	Low	Low	Low	Low
BBB permeant	No	No	No	No	NO	No
P-Gp substrate	No	No	No	No	No	No
Cyp1A2 inhibitor	No	No	Yes	No	No	No
Cyp2C19 inhibitor	No	No	Yes	No	No	No
Cyp2C9 inhibitor	Yes	Yes	Yes	Yes	Yes	Yes
Cyp2D6 inhibitor	No	No	No	No	No	No
Cyp3A4 inhibitor	Yes	Yes	Yes	Yes	Yes	Yes
Lipinski rule	2 violations	2 violations	2 violations	2 violations	2 violations	2 violations
Bioavailability score	0.17	0.17	0.17	0.17	0.17	0.17
Synthetic accessibility	5.04	4.93	4.91	4.95	5.01	4.79
Leadlikeness violations	No; 3 violations: MW > 350, rotors>7, XLOGP3 > 3.5	No; 3 violations: MW > 350, rotors>7, XLOGP3 > 3.5	3 (mw > 350, rotors>7, Xlogp3 > 3.5)	No; 3 violations: MW > 350, rotors>7, XLOGP3 > 3.5	No; 3 violations: MW > 350, rotors>7, XLOGP3 > 3.5	No; 2 violations: MW > 350, rotors>7

electrostatic interactions and enhances hydrogen-bond donar/acceptor capacity, strengthening with key AKT1 residues such as Lys64, Leu62, Ile19, and Gln79, as seen in docking data. These interactions stabilize the ligand-protein complex, contributing to their superior anticancer potential. Furthermore, the electron-withdrawing groups increase overall lipophilicit, facilitating membrane permeability and effcient cellular uptake, which enhances itracellular activity and target engagement [1–3].

The sulfonamide group, common to all derivatives, proved essential for biological activity. It provides a polar linker capable of forming dual hydrogen bond donors and acceptors promoting specific interaction with hinge region of AKT1 and contributing to higher selectivity and inhibitory potency by optimizing molecular alignment within the AKT1 binding pocket. Compounds A1, A5 and A6, which showed multiple hydrogen bonds with residues including Leu62,lys64, and Gln79, correspondingly displayed the lowest IC50 values (0.069–3.76 μM). The aromatic/lipophilic rings were also critical for π-π stacking and hydrophobic contact with Phe73,Tyr18, and Trp80, interactions that are characteristic of AKT1 inhibition. For example compound A1 displayed extensive π-π/ π-alkyl interactions with Phe73 and Tyr18, consistent with its strong binding energy (−6.8 kcal/ mol) and high cytotoxic efficacy. In contrast A2, A3 and A7 which contained less favorable or sterically hindered aromatic substituents, exhibited weaker hydrophobic interactions and higher IC50 values. Furthermore, comparison with refernce compounds AG and AG-CHO confirmed that the incorporation of substituents with electrone-withdrawing capability and heterocyclic moieties markedly enhances AKT1 binding and anticancer activity. AG-CHO, bearing an aldehyde group, showed improved potency over AG, suggesting that polar substituents facilitate optimal orientation and electron distribution within the active site. Overall these observations confirm that; 1. Electron with drawing heterocyclic substituents enhances AKT1 activity. 2. The sulfonamide is indispensible for hydrogen

Table 3
Comparative Analysis of interaction profiles and docking energies for AKT1 complexes with Compounds A1–A7, AG, and AG-CHO.

Compound	Binding interaction (amino acid residues)	Type of bonding	Distance (Å)	Docking score (kcal/Mol)
A1	Ile19	Hydrogen bond	1.86	−6.8
	Thr82	Hydrogen bond	2.26	
	Glu17	Hydrogen bond	2.26	
	Gln79	Hydrogen bond	2.74	
	Val4	Hydrophobic	4.23	
	Ile74	Hydrophobic	3.68	
	Leu62	Hydrophobic	2.44	
	Phe73	Hydrophobic	4.27	
	Phe73	π–π / π–alkyl	4.27	
	Tyr18	π–π / π–alkyl	3.46	
	Trp80	π–π / π–alkyl	4.86	
A2	Arg23	Hydrogen bond	2.84	−6.1
	Arg23	Hydrogen bond	2.99	
	Gln79	Hydrogen bond	2.99	
	Leu62	Hydrogen bond	2.26	
	Ile74	Hydrophobic	3.68	
	Leu52	Hydrophobic	3.69	
	Leu62	Hydrophobic	2.44	
	Tyr18	π–π / π–alkyl	3.67	
	Phe55	π–π / π–alkyl	4.42	
	Phe73	π–π / π–alkyl	4.27	
A3	Arg23	Hydrogen bond	4.05	−6.4
	Asn53	Hydrogen bond	2.98	
	Arg25	Hydrogen bond	3.05	
	Arg23	Hydrogen bond	3.07	
	Ile19	Hydrophobic	4.22	
	Leu52	Hydrophobic	3.54	
	Val4	Hydrophobic	4.23	
	Tyr38	π–π / π–alkyl	3.64	
	Tyr18	π–π / π–alkyl	4.95	
	Phe73	π–π / π–alkyl	4.27	
A4	Ile19	Hydrogen bond	3.80	−6.8
	Thr82	Hydrogen bond	2.24	
	Glu17	Hydrogen bond	4.45	
	Gln79	Hydrogen bond	3.06	
	Val4	Hydrophobic	4.23	
	Tyr18	Hydrophobic	3.74	
	Tyr18	π–π / π–alkyl	3.74	
	Phe73	π–π / π–alkyl	4.27	
	Phe55	π–π / π–alkyl	5.09	
A5	Asp108	Hydrogen bond	3.51	−6.5
	Ile19	Hydrogen bond	2.86	
	Gln79	Hydrogen bond	2.98	
	Lys14	Hydrogen bond	3.02	
	Val4	Hydrophobic	4.23	
	Ile74	Hydrophobic	3.68	
	Leu62	Hydrophobic	2.44	
	Phe73	Hydrophobic	4.27	
	Tyr18	π–π / π–alkyl	3.57	
	Phe73	π–π / π–alkyl	4.27	
A6	Lys64	Hydrogen bond	3.84	−6.2
	Leu62	Hydrogen bond	2.26	
	Lys64	Hydrogen bond	2.26	
	Ile74	Hydrophobic	2.74	
	Ile74	Hydrophobic	3.68	
	Leu62	Hydrophobic	2.44	
	Phe73	π–π / π–alkyl	4.27	
A7	Arg23	Hydrogen bond	3.96	−6.0
	Thr87	Hydrogen bond	2.93	
	Val83	Hydrogen bond	3.11	
	Arg15	Hydrogen bond	3.36	
	Ile74	Hydrophobic	3.68	
	Ile84	Hydrophobic	3.81	
	Pro68	Hydrophobic	4.23	
	Tyr18	Hydrophobic	3.69	
	Val83	Hydrophobic	4.47	
	Tyr18	π–π / π–alkyl	3.69	
	Phe73	π–π / π–alkyl	2.74	
AG	Ile74	Hydrogen bond	2.74	−5.4
	Leu62	Hydrogen bond	2.26	
	Lys64	Hydrogen bond	2.26	
	Phe73	π–π / π–alkyl	4.27	
	Ile74	Hydrophobic	3.68	
	Leu62	Hydrophobic	2.44	
AG-CHO	Leu62	Hydrogen bond	2.26	−5.7
	Lys64	Hydrogen bond	2.44	
			2.74	
	Ile74	Hydrogen bond		
	Phe73	π–π / π–alkyl	4.27	
	Tyr38	π–π / π–alkyl	3.57	
	Ala50	Hydrophobic	3.60	
	Leu52	Hydrophobic	3.84	
	Pro42	Hydrophobic	4.16	
	Pro51	Hydrophobic	4.16	
	Tyr38	Hydrophobic	3.59	

bonding and molecular stabilization. 3. Aromatic π-π stacking with residues such as Phe 73 and Tyr18 contributes significantly to cytotoxic potency. Thus, the intergration of structural modifications, docking analysis, and *invitro* data provides a consistent SAR model explaining the improved activity of the heterocyclic dihydropyridine-sulfonamide scaffold.

3.10. Chemistry

1,4-Dihydropyridines (1,4-DHPs) are unique cyclic compounds that are both synthetically attractive and bioactive. The 1,4-DHPs owe this chemical interest to their unique and interesting chemical structure and associated physicochemical properties. The 1,4-DHPs have been found to act as calcium channel blockers [39]. Nevertheless, the 1,4-DHPs have been found to exhibit wide-ranging biological and pharmacological activities [40–42]. During the last two decades, the growing interest in the anticancer activity of 1,4-DHPs is due to their ability to overcome multidrug resistance in cancer as well as potentiate the anticancer and antimetastatic effects of some cytotoxic agents [43–45]. It is well known that the derivatives of sulfamide have anticancer potential. Sulfonamides, a type of sulfa drug, have demonstrated some ability to suppress

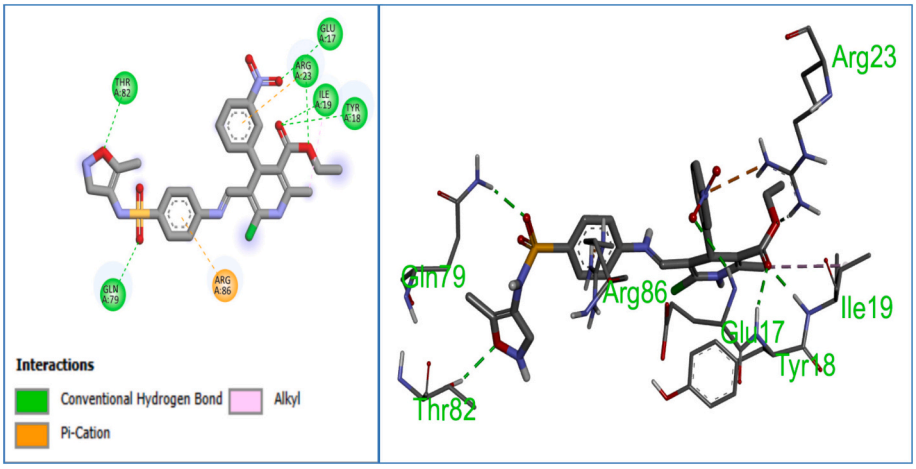

Fig. 11. Predicted binding interactions of compound A1 within the AKT1 active site. (A) The 3D structure shows the binding pose of A1 in the AKT1 active pocket, illustrating hydrogen bonds with Thr82, glu17, and Gln79 (green dashed line), a π-cation interaction with Arg86 (orange dashed line), and alkyl contacts with Ile11 and Tyr18 (purple dashed lines). (B) 2D interaction diagram illustrating conventional hydrogen bonds, π-cation interaction, and hydrophobic contact with key active site residues. (For interpretation of the references to colour in this figure legend, the reader is referred to the web version of this article.)

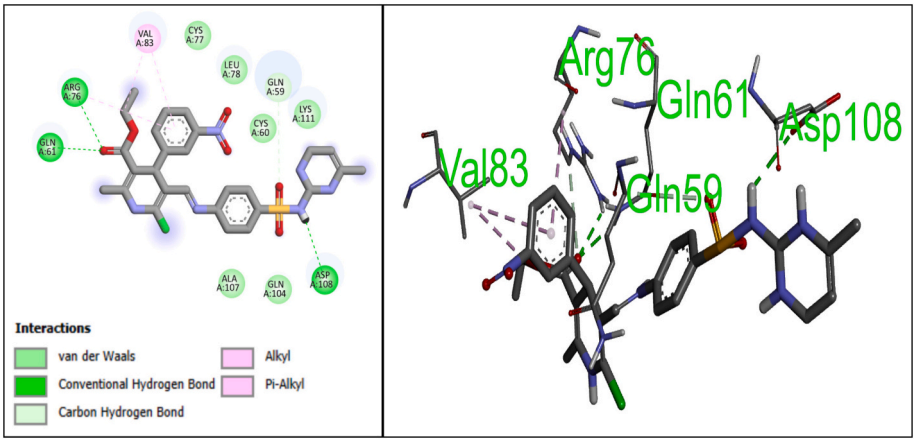

Fig. 12. Predicted binding interactions of compound A5 within the AKT1 active site. (A) The 3D docking pose illustrates how compound A5 fits into the AKT1 binding pocket, forming hydrogen bonds with Glu17, Gln79, and Thr82 (Green dashed lines), A π-cation interaction with Arg86 (orange dashed line, while hydrophobic (alkyl and π-alkyl) interactions occur with Ile19, Tyr18, Arg23, and Phe55 (purple dashed lines). (B) The 2D interaction diagram summarizes these molecular contacts, showing conventional hydrogen bonds, π-cation interaction, and hydrophobic interactions within The AKT1 active site. (For interpretation of the references to colour in this figure legend, the reader is referred to the web version of this article.)

the growth of cancer cells as well as initiate apoptosis. Sulfa compounds are also used to treat bacterial infections [46–48]. Therefore, we joined sulfonamide derivatives with the 1,4-DHPs to produce modified 1,4-DHPs sulfonamide drug compounds. This data has led to the synthesis and detailed study of a range of novel sulfamide-DHP derivatives (A1-A7). This decision was made to learn more about this group of compounds that are effective against cancer cells, which are the leading cause of death. Scheme 1 represents the general pathway of the derivatives' synthesis. The synthesis of target compounds is a multistep process. In the first step, the 3,4-dihydropyridone (AG) is obtained by a condensation of equimolar quantities of Meldrum's acid, methyl acetoacetate, ammonium acetate, and m-nitrobenzaldehyde. The mixture was heated under reflux for 12 h using acetic acid as the solvent, yielding 64 %. To make AG-DHP, compound AG was mixed with $POCl_3$ and DMF (the Vilsmeier-Haack reagent) in DCM, which was used as a solvent. After 24 h of stirring at room temperature, a solution of 16 g of sodium acetate (NaOAc) in 24 mL of water was added slowly with continued stirring for 1 h. AG-CHO was collected by filtration, with the result of the output being 68 %. The target sulfamide-DHP derivatives were obtained in the last step through the condensation of corresponding sulfonamide derivatives (sulfamethazole, sulfathiazole, sulfadiazine, sulfapyridine, sulfamerazine, sulfacetamide, and sulfanilamide) with compound AG-CHO to produce (A1-A7), respectively, from the reaction of sulfanimid derivatives with AG-DHP in a 1:1 mol ratio, using a few drops of acetic acid as a catalyst under reflux conditions for 12 h. The yield of sulfamide-DHP derivatives (A1-A7) products is within the range of 58 % to 79 %. The synthesized compounds were characterized using IR spectroscopy, electron impact mass spectrometry, and proton carbon nuclear magnetic resonance spectroscopy, as well as elemental analysis (CHNS), and these results confirm the proposed structures of the synthesized copounds.

3.11. Spectroscopic characterization

The bands of functional groups were found in the predicted regions. This was confirmed by the IR spectra of the prepared compounds (Supplementary Material Fig. S1-S9). The spectrum of AG exhibits bands at 3234 cm^{-1}, which are assigned to the NH form, and bands at 1679

cm^{-1} and at 1631 cm^{-1} which are attributed to the carbonyl groups, in addition to the bands of C—H aliphatic and aromatic groups. The spectrum of compound AG-CHO has a band at 1701 and 1649 cm^{-1} attributed to the carbonyl group. The spectra of the dihydropyridine sulfonamide derivatives (A_{1-7}) show bands for the major functional groups within the following ranges: In the range (3406–3209) cm^{-1} which are assigned to the NH of the DHP ring and NH of sulfonamide. The bands in the ranges (1707–1655) cm^{-1} are attributed to the carbonyl of ester groups, and at (1360–1340) cm^{-1}, (1165–1141) cm^{-1}, which are attributed to the SO_2 groups.

The ^{1}H NMR spectra (Supplementary Material Figs. S10-S18) show signals that match with the proposed structures for the compounds in DMSO-d_6 at 25 °C. The^{1}HNMR spectrum of the AG compound displays the signal for NH of the DHP ring at 10.7 ppm, the signals in the range of δ 8.09–7.63 ppm for the aromatic protons, and signals at δ 4.01, 2.35, and δ 1.09 ppm for the OCH_2, CH_3 and OCH_2CH_3, respectively. The spectrum of AG-CHO shows the same signals of compound AG as well as a characteristic signal for the CHO proton at δ 9.86 ppm. The^{1}HNMR spectra of A_{1-7} compounds show three characteristic signals: the first signal in the range of δ 11.48–11.66 ppm for NH of the sulfonamide

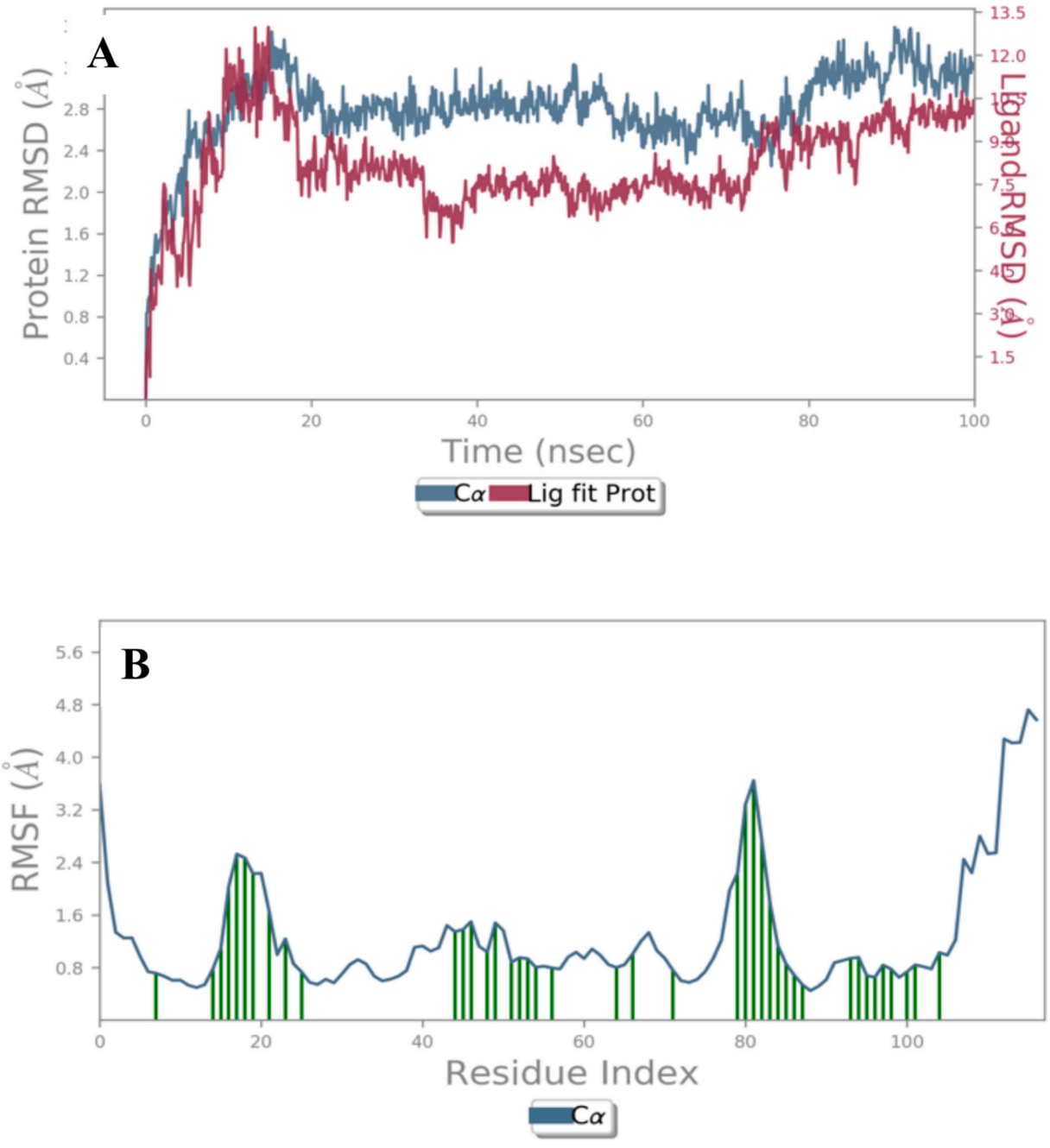

Fig. 13. Root Mean Square Deviation (RMSD) and Root Mean Square Fluctuation (RMSF) analyses of AKT1 complexes with ligand A1 and A5. (A) Protein and ligand RMSD plot for the AKT1-A1 complex over 100 ns. The protein backbone shows stable fluctuations within 1–3 A°, while the ligand remains tightly bound with low RMSD. (B) Protein RMSF plot for AKT1-A1, highlighting residue-level fluctuations. Higher flexibility is observed at terminal and loop regions, while ligand-interacting residues exhibit low RMSF. (C) Protein and ligand RMSD plot for the AKT1-A5 complex. The protein remains stable, and the ligand shows slightly higher RMSD compared to A1. (D) Protein RMSF plot for AKT1-A5, showing similar fluctuation trends to A1, with slightly lower RMSF in key binding site residues, indicating enhanced rigidity induced by ligand A5.

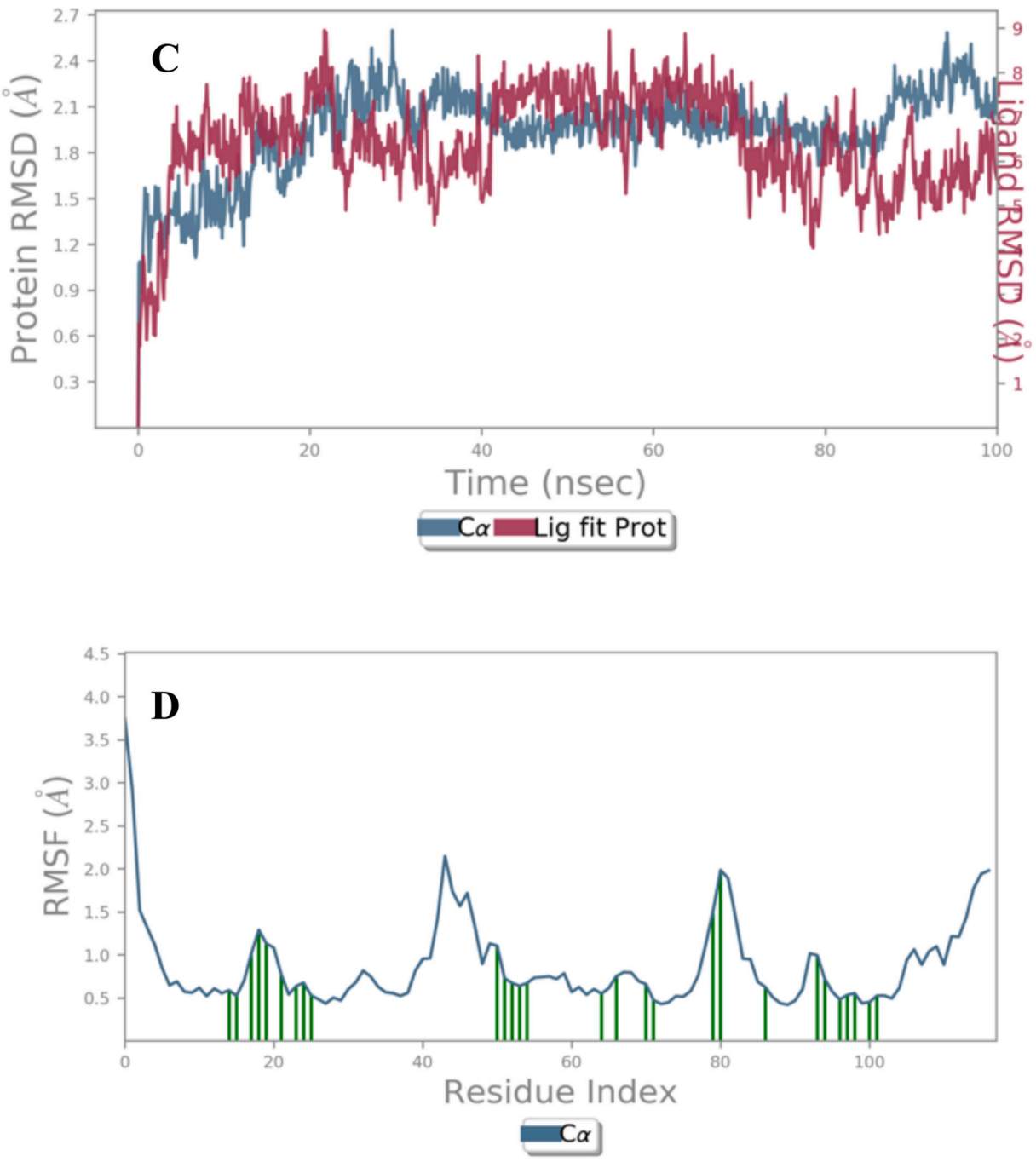

Fig. 13. (*continued*).

group NH-SO_2, the second signal in the range of δ 10.56–10.60 ppm for NH of dihydropyridine, and a third signal in the range of δ 8.48–8.91 ppm for the azomethine proton CH═N. In addition to those, the spectra contain signals of aromatic, DHP, and OCH_2CH_3 protons.

The ^{13}C NMR spectra of the synthesized compounds were given (Supplementary Material Fig. S19-S27), which revealed the expected structure of the target compounds. The ^{13}C NMR spectrum of compound AG revealed the carbon signal of the C═O amide at δ 169.8 ppm. The signal is at δ 166.8 ppm, due to the carbonyl carbon of the ester, and is consistent with the signal from other carbons. The spectrum of AG-CHO reveals a new signal for CHO at δ 187 ppm with the disappearance of the signal of the carbonyl of amide. The spectra of the dihydropyridine sulfonamide derivatives (A1–7) show an important signal for the azomethine group CH═N at the range δ 163.4–157 ppm, with the appearance of other signals, which can be assigned to the other carbon atoms in the compound. The results of ^{1}H and ^{13}C NMR spectra confirmed the expected structure of the synthesized compounds. The molecular ion peaks of the synthesized compounds were ascertained using mass spectrometry (Supplementary Material Fig. S28-S36). The intensity of the peak is indicative of the stability of the fragment, especially when the base peak is concerned. The molecular ion confirms the proposed structural elucidation.

4. Conclusion

In this study, anew series of sulfamide derivatives coupled with dihydropyridine (DHP) scaffolds were successfully synthesized and structurally characterized using IR, ^{1}H NMR, ^{13}C NMR, and mass

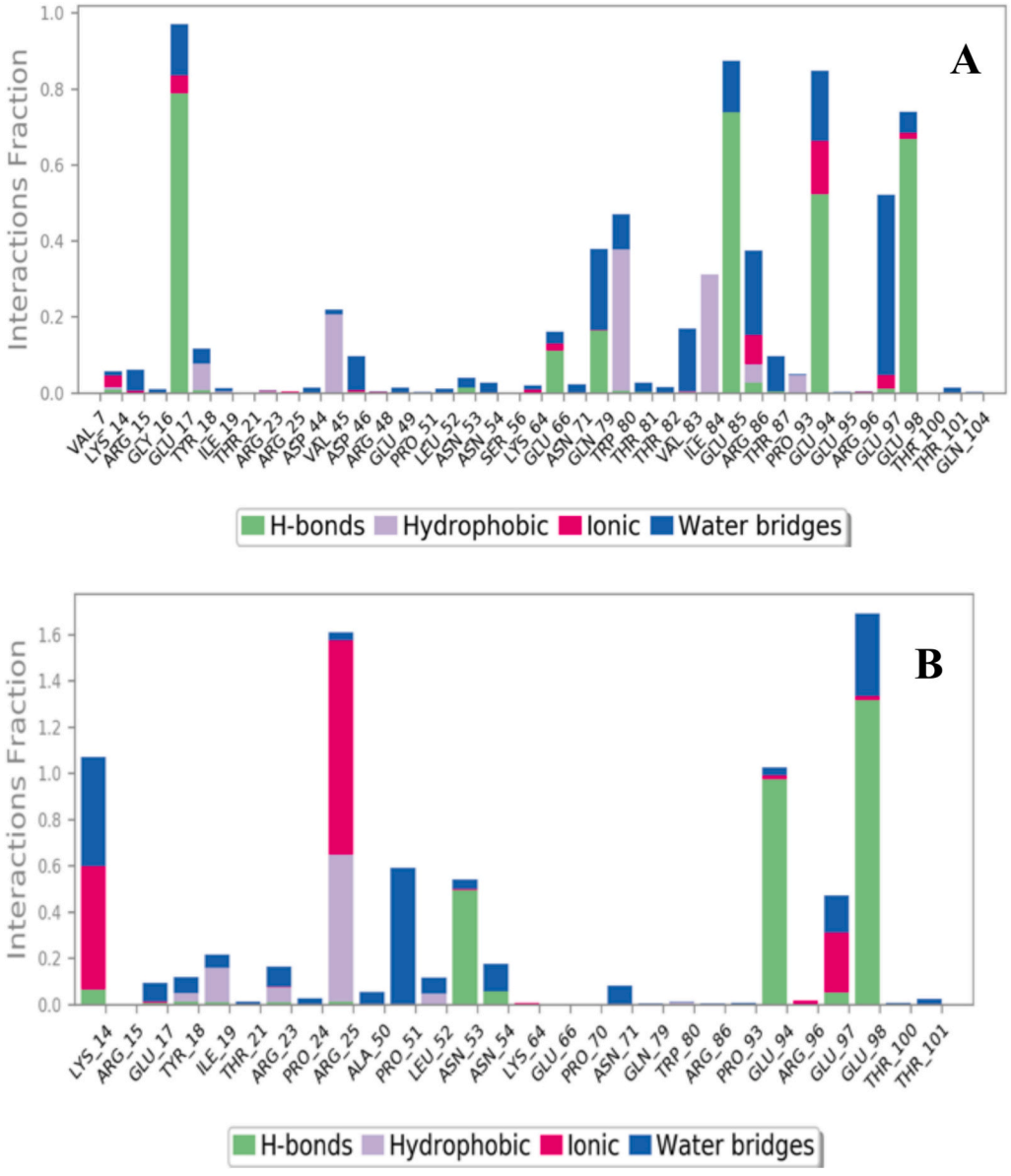

Fig. 14. Protein-ligand interaction timeline and residue -level contact maps for A1 and A5 (A) protein-ligand timeline for the AKT1-A1 complex over 100 ns, showing the total number of specific interactions. (B) protein-ligand timeline for the AKT1-A5 complex over 100 ns, showing the total number of specific interactions. (C) Residue-level interaction map for A1, highlighting specific AKT1 residues that formed contacts with the ligand for >30 % of the simulation time. Darker orange shading represents multiple or more frequent contacts. (D) Residue-level interaction map for A4, showing more widespread and consistent engagement of key residues across the binding site relative to A1.

spectrometry. The synthesized compounds were screened for anticancer efficacy on several cancer cell lines (MCF-7, A549, SKOV-3, and EA. hy926) with different levels of cytotoxicity. Flow cytometry verified apoptosis induction and cell cycle modulation, confirming the mechanistic relevance of the compound. Degree in silico analyses were performed for ADMET profiling, molecular docking and MD simulations to characterize the different binding behavior and pharmacokinetic potential of synthesized molecules and observed significant differences between the synthesized molecules. MD simulation analysis of A1 and A4 ligands with AKT1 confirmed that the complexes formed were stable across ligands, but A4 showed higher degree of protein stability, more stability and a spectrum of ligand interaction, and more affinity for new ligands. These observations were endorsed by reduced residue variation at the binding site regions, extended retention of secondary structure and increased torsional freedom in A4 over A1. However, despite poor oral bioavailability limitations of the compounds seen from the physicochemical and ADMET parameters considering their higher molecular weight and high TPSA profile, A4 exhibited promising properties as lead candidates with improved interaction stability and molecular dynamics behavior.

Overall, this integrative approach combining synthesis, biological evaluation, and computational modeling provides valuable insight into

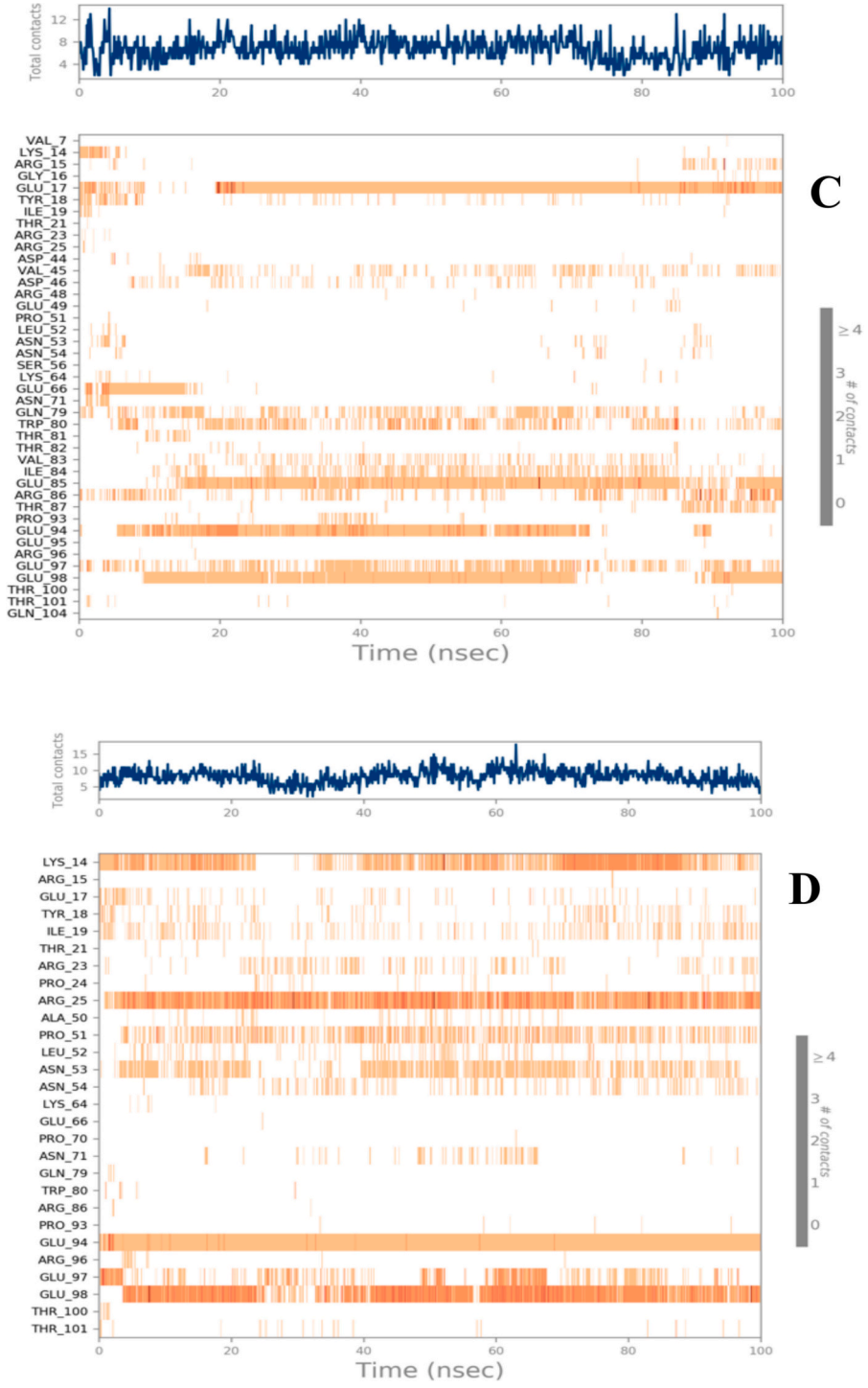

Fig. 14. (*continued*).

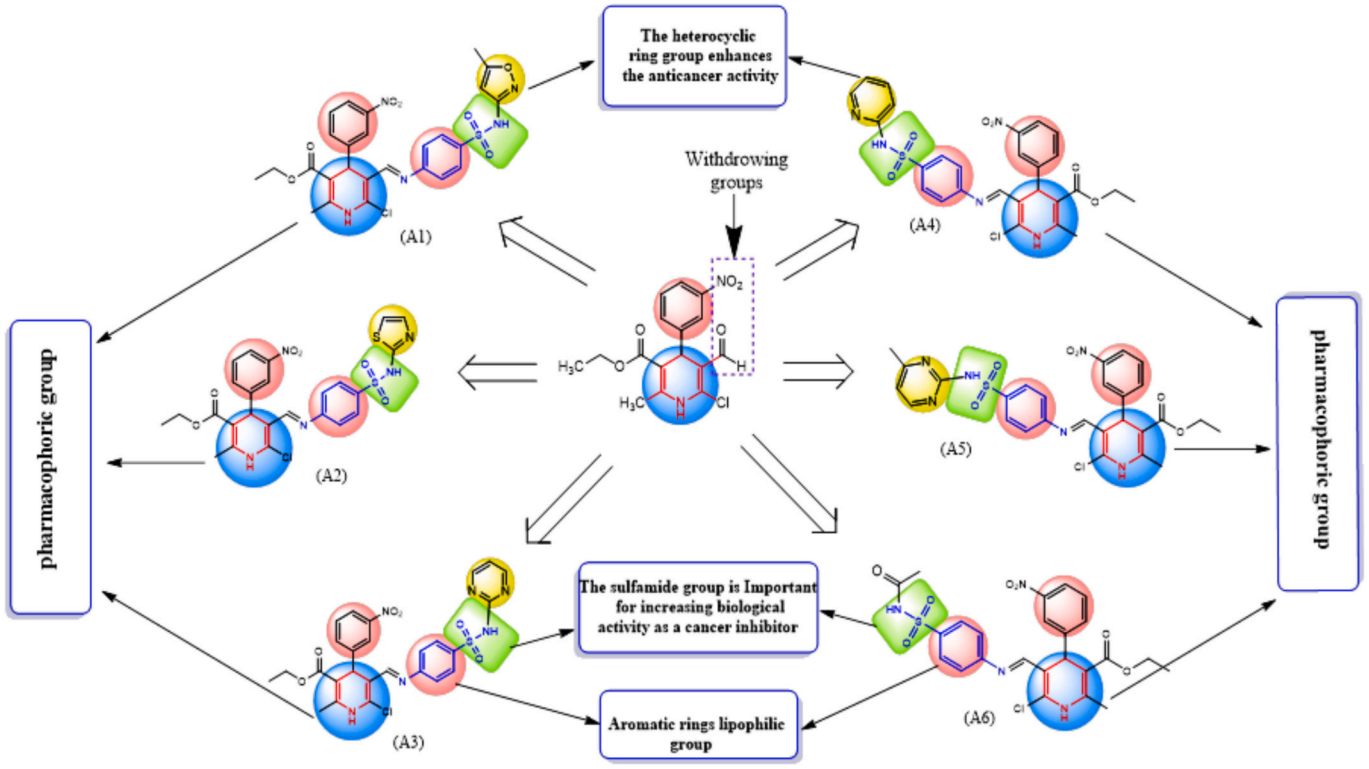

Fig. 15. Structure-activity relationship (SAR) of synthesized compounds showing key pharmacophoric features linked to anticancer activity. The yellow-highlighted heterocyclic ring groups enhance anticancer potency. Electron-withdrawing groups (e.g., -NO2) further modulate activity, while the green-highlighted sulfamide groups increase biological activity as cancer inhibitors. The pink-highlighted aromatic rings serve as lipophilic groups that promote molecular interactions with the biological target. (For interpretation of the references to colour in this figure legend, the reader is referred to the web version of this article.)

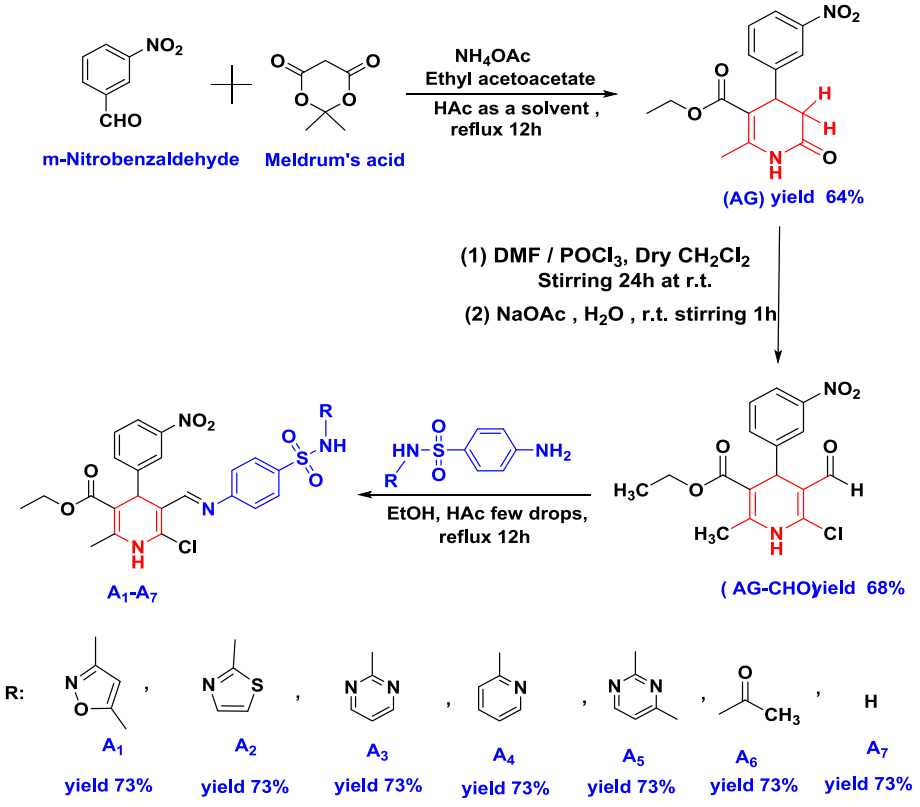

Scheme 1. The Pathway of Synthesis of 1,4-Dihydropyridine sulfamide derivatives

the design of DHP-sulfonamide hybrids as potential anticancer agents. Further optimization and in vivo validation are warranted to advance these compounds toward clinical relevance.

CRediT authorship contribution statement

Amjed Abdulrasool: Writing – review & editing, Writing – original draft, Visualization, Methodology, Investigation, Formal analysis, Data curation, Conceptualization. **Aymen G. Faisel:** Writing – review & editing, Software, Resources, Project administration, Methodology, Investigation, Data curation. **Ruaa Q. Ibrahim:** Writing – review & editing, Software, Resources, Project administration, Methodology, Investigation, Funding acquisition, Formal analysis, Data curation, Conceptualization. **Tahseen A. Alsalim:** Writing – original draft, Methodology, Formal analysis, Conceptualization. **Dunya AL-Duhaidahawi:** Writing – original draft, Visualization, Methodology, Investigation, Data curation. **Ahmed A. Majed:** Writing – review & editing, Writing – original draft, Visualization, Validation, Resources, Methodology, Funding acquisition, Formal analysis, Data curation, Conceptualization. **Nehad H. Gad:** Writing – original draft, Visualization, Software, Project administration. **Mohammad Y. Alfaifih:** Writing – review & editing, Visualization, Validation, Supervision, Software, Project administration, Investigation, Conceptualization. **Ali A. Shatii:** Writing – original draft, Visualization, Investigation, Funding acquisition, Formal analysis, Data curation. **Serag Eldin I. Elbehairii:** Writing – review & editing, Software, Resources, Project administration, Methodology, Investigation, Funding acquisition, Formal analysis, Data curation, Conceptualization. **Ahmed M. Hussein:** Writing – review & editing, Writing – original draft, Visualization, Validation, Supervision, Software, Resources, Data curation. **Fatih Alioglu:** Writing – original draft, Methodology, Formal analysis, Data curation. **Mohammed Aufy:** Writing – review & editing, Visualization, Validation, Supervision, Software, Project administration, Investigation, Conceptualization.

Declaration of competing interest

The authors declare that they have no known competing financial interests or personal relationships that could have appeared to influence the work reported in this paper.

Acknowledgement

The authors extend their appreciation to the University Higher Education Fund for funding this research work under Research Support Program for Central labs at King Khalid University through the Project number (CL/CO/B/3).

Appendix A. Supplementary data

Supplementary data to this article can be found online at https://doi.org/10.1016/j.bioorg.2025.109393.

Data availability

Data will be made available on request.

References

[1] J. Ferlay, S. Hai-Rim, F. Bray, D. Forman, C. Mathers, D.M. Parkin, Int. J. Cancer 127 (2010) 2893–2917.
[2] G.A. Rehab, A.A. Heider, A. Sabah, A.M. Ahmed, A.A. Ahmed, A. Ayat, A. A. Tahseen, Anti-breast Cancer potential of new indole derivatives: synthesis, in-silico study, and cytotoxicity evaluation on MCF-7 cells, J. Mol. Struct. 1326 (2025) 141176, https://doi.org/10.1016/j.molstruc.2024.141176.
[3] N.M. Nasir, T.A. Alsalim, A.A. El-arabey, M. Abdalla, Anticancer, antioxidant activity and molecular docking study of thiazolidine-4-one and thiadiazole derivatives, J. Biomol. Struct. Dyn. 41 (2022) 3976–3992, https://doi.org/10.1080/07391102.2022.2060306.
[4] F. Bray, M. Laversanne, H. Sung, J. Ferlay, R.L. Siegel, I. Soerjomataram, A. Jemal, Global cancer statistics 2022: GLOBOCAN estimates of incidence and mortality worldwide for 36 cancers in 185 countries, CA Cancer J. Clin. 74 (2024) 229–263, https://doi.org/10.3322/caac.21834.
[5] D. Hanahan, R.A. Weinberg, Hallmarks of cancer: the next generation, Cell 144 (2011) 646–674, https://doi.org/10.1016/j.cell.2011.02.013.
[6] Y. Chen, X. You, L. Ye, S. Mei, J. Yu, Y. Xie, K. Wang, X. Chen, Electrodeposited zinc oxide nanoparticles: synthesis, characterization, and anti-cervical cancer effects, Arab. J. Chem. 17 (2024) 105992, https://doi.org/10.1016/j.arabjc.2024.105992.
[7] (a) F. Bray, J. Ferlay, I. Soerjomataram, R.L. Siegel, L.A. Torre, A. Jemal, Global cancer statistics 2018: GLOBOCAN estimates of incidence and mortality worldwide for 36 cancers in 185 countries, CA Cancer J. Clin. 68 (2018) 394–424, https://doi.org/10.3322/caac.21492;
(b) M.A. Ahmed, A.S. Dawood, Synthesis of some newthiazolidine and 1,3,4-oxadiazole derived from L-cysteine andstudy their biological activity as antioxidant and Breast cancer, Lett. Appl. NanoBioscience 12 (2023) 82, https://doi.org/10.33263/LIANB S123.082.
[8] Z.H. Mahdi, T.A. Alsalim, H.A. Abdulhussein, A.A. Majed, S. Abbas, Synthesis, molecular docking, and anti-breast cancer study of 1-H-indol-3-Carbohydrazide and their derivatives, Results Chem. 11 (2024) 101762, https://doi.org/10.1016/j.rechem.2024.101762.
[9] V. Schirrmacher, S. van Gool, W. Stuecker, Breaking therapy resistance: an update on oncolytic Newcastle disease virus for improvements of Cancer therapy, Biomedicines 7 (2019) 66, https://doi.org/10.3390/biomedicines7030066.
[10] Q.A. Abdalzahra, A.A. Majed, Z.K. Al-Khazragia, D.S. Abid, H.H. Nameh, S. Abbas, A. Obid, A.A. Al-Khafagi, A.A. Al-Mutairi, M.E.A. Zaki, S.A. Al-Hussain, S. M. Gomha, I.M. Abdellah, A. Elhenawy, Integrated experimen-tal and computational insights into thiazolidine derivatives with potent cytotoxicity against PC-3 prostate cancer cells, Mater. Chem. Phys. 345 (2025) 131256, https://doi.org/10.1016/j.match emphys.2025.131256.
[11] J. Zhao, J. Carbone, G. Farruggia, A. Janecka, L. Gentilucci, N. Calonghi, Synthesis and Antiproliferative activity against Cancer cells of indole-aryl-AmideDerivatives, Molecules 28 (2023) 265, https://doi.org/10.3390/molecules28010265.
[12] A.A. Singh, M.P. Patil, M. Kang, I. Niyonizigiye, G. Kim, Biomedical application of Indole-3-carbinol: A mini-review, Phytochem. Lett. 41 (2021) 49–54, https://doi.org/10.1016/j.phytol.2020.09.024.
[13] S.F.A. Tahseen, M.S.A. Hamid, A.M. Ahmed, H.M. Mustafa, S. Eman, A. Radwan, Synthesis, breast cancer activity, molecular docking and dynamic simulation of 1,4-dihydropyridine derivatives, J. Mol. Struct. 1321 (2025) 139704, https://doi.org/10.1016/j.molstruc.2024.139704.
[14] Z. Ling, Y. Hao, D. Liang, C.L. Zhang, Y.F. Liu, Y. Wang, The expanding role of pyridine and Dihydropyridine scaffolds in drug design, Drug Des. Devel. Ther. 13 (2021) 4289–4338, https://doi.org/10.2147/DDDT.S329547.
[15] J.E. Blower, M.T. Ma, F. Al-Salemee, A.D. Gee, The Hantzsch reaction for nitrogen-13 PET: preparation of [^{13}N]nifedipine and derivatives, Chem. Commun. (Camb.) 57 (2021) 4962–4965, https://doi.org/10.1039/d1cc00495f.
[16] A. Hantzsch, Condensationsprodukte aus Aldehydammoniak und ketonartigen Verbindungen, Ber. Dtsch. Chem. Ges. 14 (1881) 1637–1638, https://doi.org/10.1002/cber.18810140214.
[17] J. Chasák, I. Janicki, L. Brulíková, The Liebeskind–Srogl cross-coupling reaction towards the synthesis of biologically active compounds, Eur. J. Med. Chem. 290 (2025) 117526, https://doi.org/10.1002/chem.202501664.
[18] V. Eynde, J. Jacques, A. Mayence, Synthesis and aromatization of Hantzsch 1,4-Dihydropyridines under microwave irradiation. An overview, Molecules 8 (2003) 381–391, https://doi.org/10.3390/80400381.
[19] A. Goswami, N. Kaur, M. Kaur, K. Singh, H.S. Sohal, H. Han, P.K. Bhowmik, Facile one-pot synthesis and anti-microbial activity of novel 1,4-Dihydropyridine derivatives in aqueous micellar solution under microwave irradiation, Molecules 29 (2024) 1115, https://doi.org/10.3390/molecules29051115.
[20] I.V. Machado, J.R.N. dos Santos, M.A.P. Januario, A.G. Corrêa, Greener organic synthetic methods: Sonochemistry and heterogeneous catalysis promoted multicomponent reactions, Ultrason. Sonochem. 78 (2021) 105704, https://doi.org/10.1016/j.ultsonch.2021.105704.
[21] G.B. Dharma, Hantzsch reaction: A greener and sustainable approach to 1,4-Dihydropyridines using non-commercial β-Ketoesters, J. Heterocyclic Chem. 55 (2018) 2556–2562, https://doi.org/10.1002/jhet. 3309.
[22] J. Rahimi, M. Niksefat, M. Heidari, M. Naderi, H. Abbasi, I. Tajik, A. Maleki Ali, Ammonium metavanadate (NH_4VO_3): a highly efficient and eco-friendly catalyst for one-pot synthesis of pyridines and 1,4-dihydropyridines, Sci. Rep. 12 (2022), https://doi.org/10.1038/s41598-022-17378-7.
[23] S.T. Shinde, K.G. Kanade, R.B. Gawade, V.B. Hinge, M.D. Shinde, D.B. Bankar, N. M. Thorat, D.P. Amalnerkar, $AlCl_3$@ZnO nanostructured material: an efficient green catalyst for the one-pot solvent-free synthesis of 1,4-dihydropyridines, RSC Adv. 13 (2023) 24767–24776, https://doi.org/10.1039/D3RA04277D.
[24] M.G. Sharma, D.P. Rajani, H.M. Patel, Green approach for synthesis of bioactive Hantzsch 1,4-dihydropyridine derivatives based on thiophene moiety via multicomponent reaction, R. Soc. Open Sci. 4 (6) (2017) 1–8, https://doi.org/10.1098/rsos.170006.
[25] C.T. Supuran, A. Casini, A. Scozzafava, Protease inhibitors of the sulfonamide type: anticancer, antiinflammatory, and antiviral agents, Med. Res. Rev. 23 (2003) 535–558.
[26] H. Otten, Domagk and the development of the sulphonamides, J. Antimicrob. Chemother. 17 (1986) 689–690, https://doi.org/10.1093/jac/17.6.689.
[27] D. Fernández-Villa, M.R. Aguilar, L. Rojo, Folic acid antagonists: antimicrobial and Immunomodulating mechanisms and applications, Int. J. Mol. Sci. 20 (2019) 4996, https://doi.org/10.3390/ijms20204996.

[28] C.T. Supuran, F. Briganti, S. Tilli, W.R. Chegwidden, A. Scozzafava, Carbonic anhydrase inhibitors: sulfonamides as antitumor agents? Bioorg. Med. Chem. 9 (2001) 703–714, https://doi.org/10.1016/S0968-0896(00)00288-1.
[29] D. Vullo, M. Franchi, E. Gallori, J. Pastorek, A. Scozzafava, S. Pastorekova, C. T. Supuran, Carbonic anhydrase inhibitors: inhibition of the tumor-associated isozyme IX with aromatic and heterocyclic sulfonamides, Bioorg. Med. Chem. Lett. 13 (2003) 1005–1009, https://doi.org/10.1016/s0960-894x(03)00091-x.
[30] M.Y. Moskalik, Sulfonamides with Heterocyclic Periphery as Antiviral Agents, Molecules 28 (51) (2022), https://doi.org/10.3390/molecules28010051.PMID: 36615245;PMCID:PMC9822084.
[31] M. Abdelrahman, W. Eldehna, A. Nocentini, H. Ibrahim, H. Almahli, H. Abdel-Aziz, S. Abou-Seri, C. Supuran, Novel benzofuran-based sulphonamides as selective carbonic anhydrases IX and XII inhibitors: synthesis and in vitro biological evaluation, J. Enzyme Inhib. Med. Chem. 35 (2019) 298–305, https://doi.org/10.1080/14756366.2019.1697250.
[32] A. García-Llorca, F. Carta, C.T. Supuran, T. Eysteinsson, Carbonic anhydrase, its inhibitors and vascular function, Front Mol Biosci. 11 (2024) 1338528, https://doi.org/10.3389/fmolb.2024.1338528.
[33] A. Giles, J. Foushee, E. Lantz, G. Gumina, Sulfonamide Allergies, Pharmacy 7 (2019) 132, https://doi.org/10.3390/pharmacy7030132.
[34] A. Dakhlaoui, F. Djouahra, H. Boussetta, et al., Exploring the potential of sulfonamide–dihydropyridine hybrids as multitargeted ligands for alzheimer's disease treatment, Int. J. Mol. Sci. 24 (2023) 9742, https://doi.org/10.3390/ijms24119742.
[35] M.O. Kaya, T. Demirci, O. Özdemir, Ü. Çalışır, F. Sönmez, M. Arslan, Synthesis, inhibition effects, molecular docking and theoretical studies as Paraoxonase-1 (PON1) inhibitors of novel 1,4-Dihydropyridine-substituted sulfonamide derivatives, Med. Chem. Res. 32 (2023) 4413–4428, https://doi.org/10.1007/s00044-023-03029-7.
[36] VulcanChem, 2-Oxo-N-(4-sulfamoylphenyl)-1,2-dihydropyridine-3-carboxamide product Page, Accessed, https://www.vulcanchem.com/product/2-oxo-n-(4-sulfamoylphenyl)-1-2-dihydropyridine-3-carboxamide, 2025.
[37] D. Viradiya, S. Mirza, F. Shaikh, et al., Design and synthesis of 1,4-Dihydropyridine derivatives as anti-cancer agent, Anti Cancer Agents Med. Chem. 17 (2017) 1003–1013, https://doi.org/10.2174/1871520616666161206143251.
[38] S. Akili, D. Ben Hadda, Y. Bitar, A. Najjar, M.F. Chehna, Computer-aid Design of Novel Sulfonamide Derivatives as EGFR kinase inhibitors for Cancer treatment, Int. J. Org. Chem. 11 (2021) 171–186, https://doi.org/10.4236/ijoc.2021.114012.
[39] Cephalon France SAS (Lafon), 1,4-Dihydropyridines à Groupe Sulfonamide., Patent FR2781224 A1, WO2000/003987; US 6166035, https://worldwide.espacenet.com/patent/search/family/013142403/publication/FR2781224A1, 1998.
[40] L. Li, X. Zhang, H. Wang, N-(Ortho Phenylamino Dihydropyridyl) Sulfonamides and N-(Ortho Phenylamino Dihydropyridyl), N′-Alkyl Sulfamides as MEK Inhibitors for Cancer Treatment., CN101454004B (2010). https://patents.google.com/patent/CN101454004B/en.
[41] K. Yamada, T. Sato, M. Matsumura, Use of sulfonamide-containing compounds in combination with angiogenesis inhibitors for, Cancer Therapy. (2014). US8772269B2, https://patents.google.com/patent/US8772269B2/en.
[42] M. Suárez, E. Salfrán, E. Ochoa, Y. Verdecia, L. Alba, N. Martín, C. Seoane, R. Martínez-Alvarez, H.N. De Armas, N.M. Blaton, O.M. Peeters, C.J. De Ranter, Structural study of highly halogenated dihydropyridine derivatives as potential calcium channel modulators, J. Heterocyclic Chem. 40 (2003) 269–275, https://doi.org/10.1002/jhet.5570400211.
[43] N. Elangovan, S. Sowrirajan, K.P. Manoj, A.M. Kumar, J. Mole. Struc. 1241 (2021) 1–10.
[44] K. Saour, D. Lafta, Synthesis of new benzimidazole and benzothiazole disulfide metal complexes as G-quadruplex binding ligands, Anti Cancer Agents Med. Chem. 16 (7) (2016) 891–897, https://doi.org/10.2174/1871520616666160204111637.
[45] J. Suhail Wadi, D. AL-Duhaidahawi, S. Salam Abdullah, M. Jabir, M.A.A. Najim, S. Farhan Jawad, S.S. Hamzah, F. Abdul Qais, Exploring the interaction between 3-D structure of TLR 9 and prostaglandin analogues, Arab. J. Chem. 16 (5) (2023) 104692, https://doi.org/10.1016/j.arabjc.2023.104692.
[46] H. Al-Kelabi, D. Al-Duhaidahawi, K. Al-Khafaji, N.A. Al-Masoudi, New tamoxifen analogs for breast cancer therapy: synthesis, aromatase inhibition and in silico studies, J. Biomol. Struct. Dyn. 41 (22) (2023) 12798–12807, https://doi.org/10.1080/07391102.2023.2175375.
[47] S. Ardevines, F. Auria-Luna, E. Romanos, et al., 1-Benzamido-1,4-dihydropyridine derivatives as anticancer agents: In Vitro and In Vivo assays, Arab. J. Chem. 16 (2023) 104514, https://doi.org/10.1016/j.arabjc.2023.104514.
[48] M.O. Kaya, T. Demirci, A.B. Musatat, et al., N-substituted sulfonamide-1,4-Dihydropyridines: experimental and theoretical evaluation as hybrid pharmacophores, Int. J. Biol. Macromol. 274 (2024) 133184, https://doi.org/10.1016/j.ijbiomac.2024.133184.

Further reading

[49] A. de Fátima Silva, D. Forti Lago, Carvalho, L. da Silva, S. Thomasi, 1,4-Dihydropyridine derivatives: an overview of synthesis conditions and biological tests, Curr. Org. Chem. 27 (2023) 1567–1610, https://doi.org/10.2174/0113852728264228231013074432.
[50] P. Anaikutti, P. Makam, 1,4-Dihydropyridine: synthetic advances, medicinal and insecticidal properties, RCS Adv. 12 (2022) 29253–29290.
[51] A. Gonzalez, J. Casado, M.G. Gunduz, B. Santos, A. Velazquez-Campoy, C. Sarasa-Buisan, M.F. Fillat, M. Montes, E. Piazuelo, A. Lanas, 1,4-Dihydropyridine as a promising scaffold for novel antimicrobials against helicobacter pylori, Front. Microbiol. 13 (2022) 874709.
[52] G. Prasanthi, K. Prasad, K. Bharathi, Design, synthesis and evaluation of dialkyl 4-(benzo d-1,3 dioxol-6-yl)-1,4-dihydro-2,6-dimethyl-1-substituted pyridine-3,5-dicarboxylates as potential anticonvulsants and their molecular properties prediction, Eur. J.Med. Chem. 66 (2013) 516–525.
[53] I. Akbar, S. Radhakrishnan, K. Meenakshisundaram, A. Manilal, A.A. Hatamleh, B. K. Alnafisi, A. Ahamed, R. Balasubramani, Design of 1,4-dihydropyridine hybrid benzamide derivatives: synthesis and evaluation of analgesic activity and their moleculardocking studies, Drug Des. Dev. Ther. 16 (2022) 4021–4039.
[54] P. Anaikutti, P. Makam, Dual active 1,4-dihydropyridine derivatives: design, green synthesis and in *vitro* anti-cancer andanti-oxidant studies, Bioorg. Chem. 105 (2020) 104379.
[55] R. Miri, R. Motamedi, M.R. Rezaei, O. Firuzi, A. Javidnia, A. Shafiee, Design, synthesis and evaluation of cytotoxicity of novelchromeno[4,3-b]quinoline derivatives, Arch. Pharm. Chem. Life Sci. 2 (2011) 111–118.
[56] Y. Wan, G. Fang, H. Chen, X. Deng, Z. Tang, Sulfonamide derivatives as potential anti-cancer agents and their SARs elucidation, Eur. J. Med. Chem. (2021) 113837, https://doi.org/10.1016/j.ejmech.2021.113837.
[57] K.A. Elsayad, G.F. Elmasry, S.T. Mahmoud, F.M. Awadallah, Sulfonamides as anticancer agents: A brief review on sulfonamide derivatives as inhibitors of various proteins overexpressed in cancer, Bioorg. Chem. 147 (2024) 107409, https://doi.org/10.1016/j.bioorg.2024.107409.